

METEORITICS & PLANETARY SCIENCE

Early Diagenesis at and below Vera Rubin ridge, Gale crater, Mars

Journal:	<i>Meteoritics & Planetary Science</i>
Manuscript ID	MAPS-3546.R2
Manuscript Type:	Article
Date Submitted by the Author:	n/a
Complete List of Authors:	Turner, Stuart; The Open University, AstrobiologyOU, School of Environment, Earth and Ecosystem Sciences Schwenzer, Susanne; The Open University, AstrobiologyOU, School of Environment, Earth and Ecosystem Sciences Bridges, John; Leicester University, Space Research Centre, School of Physics & Astronomy Rampe, Elizabeth; NASA Johnson Space Center Bedford, Candice; The Open University, School of Physical Sciences; Lunar and Planetary Institute; NASA Johnson Space Center Achilles, Cherie; NASA Goddard Space Flight Center McAdam, Amy; NASA Goddard Space Flight Center Mangold, Nicolas; LPGN/CNRS , 7. Laboratoire Planétologie et Géodynamique de Nantes Hicks, Leon; University of Leicester, Space Research Centre, School of Physics and Astronomy Parnell, John; University of Aberdeen, School of Geosciences Fraeman, Abigail; NASA Jet Propulsion Laboratory Reed, Mark; University of Oregon, Department of Geological Sciences
Keywords:	Martian, rock(s) < Martian, Mineral(s), aqueous < Alteration

SCHOLARONE™
Manuscripts

1
2
3
4 1 **Early Diagenesis at and below Vera Rubin ridge, Gale crater, Mars**

5 2 **S. M. R. Turner¹, S. P. Schwenzer¹, J. C. Bridges², E. B. Rampe³, C. C. Bedford^{3,4,5}, C. N.**
6 3 **Achilles⁶, A. C. McAdam⁶, N. Mangold⁷, L. J. Hicks², J. Parnell⁸, A. A. Fraeman⁹, M. H.**
7 4 **Reed¹⁰**

8
9
10 5 ¹AstrobiologyOU, School of Environment, Earth and Ecosystem Sciences, The Open University,
11 6 UK.

12
13 7 ²Space Research Centre, School of Physics and Astronomy, University of Leicester, UK.

14
15 8 ³NASA Johnson Space Center, USA.

16
17 9 ⁴School of Physical Sciences, The Open University, UK.

18 10 ⁵Lunar and Planetary Institute, Universities Space Research Association, USA.

19
20 11 ⁶NASA Goddard Space Flight Center, USA.

21 12 ⁷Laboratoire de Planétologie et Géodynamique, UMR6112 CNRS, Université de Nantes,
22 13 Université Angers, France.

23
24 14 ⁸School of Geosciences, University of Aberdeen, UK.

25
26 15 ⁹Jet Propulsion Laboratory, California Institute of Technology, USA.

27 16 ¹⁰Department of Earth Sciences, University of Oregon, USA.

28
29 17
30 18 Corresponding author: Stuart Turner (stuart.turner@open.ac.uk).

19 **ABSTRACT**

20 Data returned by NASA's Mars Science Laboratory *Curiosity* rover showed evidence for
21 abundant secondary materials, including Fe-oxides, phyllosilicates, and an amorphous
22 component on and below Vera Rubin ridge in the Murray formation. We used equilibrium
23 thermochemical modeling to test the hypothesis that altered sediments were deposited as detrital
24 igneous grains and subsequently underwent diagenesis. Chemical compositions of the Murray
25 formations' altered components were calculated using data returned by the Chemistry and
26 Mineralogy X-ray diffraction instrument and the Alpha Particle X-ray Spectrometer on board
27 *Curiosity*. Reaction of these alteration compositions with a CO₂-poor and oxidizing dilute
28 aqueous solution was modeled at 25 – 100 °C, with 10 – 50% Fe³⁺/Fe_{tot} of the host rock. The
29 modeled alteration assemblages included abundant phyllosilicates and Fe-oxides at water to rock
30 ratios >100. Modeled alteration abundances were directly comparable to observed abundances of
31 hematite and clay minerals at a water to rock ratio of 10,000, for system temperatures of 50 –
32 100 °C with fluid pH ranging from 7.9 to 9.3. Modeling results suggest that the hematite-clay
33 mineral assemblage is primarily the result of enhanced groundwater flow compared to the
34 Sheepbed mudstone observed at Yellowknife Bay, and underwent further, localized alteration to
35 produce the mineralogy observed by *Curiosity*.

36 INTRODUCTION

37 At Gale crater, evidence for an ancient lacustrine environment within which sediments
38 were deposited and diagenetically altered have been found in the Murray formation by the
39 NASA Mars Science Laboratory (MSL) *Curiosity* rover (e.g., Grotzinger et al., 2015; Edgar et
40 al., 2020; see Fraeman et al., 2020 for an overview of the entire geologic context). In this study
41 we use thermochemical modeling to test the hypothesis that the sediments were deposited as
42 detrital igneous grains followed by diagenetic alteration conditions where groundwater interacted
43 with the sediments. This is in continuation of previous work at the first units encountered by
44 *Curiosity* at Yellowknife Bay (Bridges et al., 2015b; Schwenzer et al., 2016). In doing so, we
45 aim to constrain associated temperature, water to rock ratios, pH, and redox conditions of the
46 early diagenetic alteration pathways that resulted in the predominantly hematite-clay mineral
47 assemblage in the Murray formation on and below Vera Rubin Ridge (VRR). We assume that
48 Ca-sulfate vein formation as described in L'Haridon et al. (2020) and acidic alteration (Rampe et
49 al., 2020b) belong to a later phase of alteration as well as Ca-sulfate formation, which has been
50 shown to occur during a later step of fluid evolution (Schwenzer et al., 2016). The former is
51 consistent with the sedimentological observations (Edgar et al., 2020) and observations by
52 *Curiosity*'s instruments (e.g., McAdam et al., 2020).

53 Overview of the Murray Formation

54 The Murray formation was first encountered on sol 792 of the NASA MSL mission and
55 constitutes the sedimentary units analyzed by the *Curiosity* rover from the foothills of Mount
56 Sharp (Grotzinger et al., 2015). From orbit, the lower Murray formation has areas with orbital
57 spectral signatures consistent with Fe/Mg clay, hydrated silica, iron oxides, and sulfate
58 (Anderson and Bell, 2010; Milliken et al., 2010; Thomson et al., 2011; Fraeman et al., 2013;
59 Fraeman et al., 2016). Distinct from orbit by its hematite spectral signature (Fraeman et al.,
60 2013), VRR is a ~200 m wide ~6.5 km long northeast-southwest resistant geomorphological
61 feature on the northern slopes of Mount Sharp (Fig. 2). VRR is composed of the Pettegrove Point
62 member that is overlain by the Jura member (Fig. 1). They have a combined stratigraphic
63 thickness of approximately 60 m and were investigated by *Curiosity* from sol 1809 to sol 2302,
64 when *Curiosity* traversed off VRR.

65 At the time of writing, the Murray formation is estimated to be ~300 m thick and has
66 been subdivided into seven members that are separated by conformable contacts, as illustrated by
67 Edgar et al. (2020). Briefly, the seven members are the Pahrump Hills, Hartman's Valley,
68 Karasburg, Sutton Island, Blunts Point, Pettegrove Point and Jura, comprised of sand- silt and
69 mudstones of lake bed and fluvial origin as detailed in the following sections (Grotzinger et al.,
70 2015; Bristow et al., 2018; Edgar et al., 2018; Fedo et al., 2018; Gwizd et al., 2018; Rivera-
71 Hernandez et al., 2019; Stack et al., 2019; Edgar et al., 2020).

72 *Summary of Murray Formation stratigraphic members below Vera Rubin Ridge*

73 Stratigraphic members below VRR of interest in this study were the Hartmann's Valley,
74 Karasburg, Sutton Island, and Blunts Point members (Fig. 1).

75 The Hartmann's Valley member (25 m thick) has grains ranging in size between silt to
76 medium sand and with meter-scale, trough cross-bedding indicative of either fluvial or aeolian
77 settings (Bristow et al., 2018; Fedo et al., 2018; Gwizd et al., 2018). The Oudam sample was

1
2
3 78 drilled from this member, in fine-grained bedrock containing diagenetic Ca-sulfate mineral veins
4 79 (Bristow et al., 2018).

5
6 80 The Karasburg member (37 m thick) in the Murray Buttes locality is characterized by a
7 81 heterolithic mudstone/fine sandstone assemblage with abundant cm-scale concretions and a
8 82 purple hue (Fedo et al., 2018). In this member, the samples Marimba and Quela were drilled
9 83 from flat mudstone bedrock containing some small Ca-sulfate mineral veins and mm-scale Mn-
10 84 enriched concretions (Bristow et al., 2018; L'Haridon et al., 2018; Meslin et al., 2018).

11
12 85 The Sutton Island member (98 m thick) also contains a heterolithic mudstone/sandstone
13 86 assemblage that is largely red in color and has an increased abundance of Ca-sulfate features
14 87 (e.g., veins and lenticular crystals) and polygonal cracks interpreted to result from desiccation at
15 88 the lake margins (Stein et al., 2018). The Sebina sample was drilled from flat, fine-grained
16 89 bedrock that has abundant, cm-scale nodules and Ca-sulfate mineral veins.

17
18 90 The Blunts Point member (~100 m thick) is exposed immediately below VRR on the
19 91 north-facing side and shares a conformable boundary with the ridge (Edgar et al., 2020; Fedo et
20 92 al., 2018). The Blunts Point member is characterized by well laminated mudstone with cross-
21 93 cutting curvilinear Ca-sulfate veins (Edgar et al., 2020). The Duluth drill sample was acquired
22 94 near the base of VRR in a well laminated bedrock with diagenetic raised ridges and Ca-sulfate
23 95 veins (Fig. 1).

24 96 *Summary of Murray Formation stratigraphic members on Vera Rubin Ridge*

25
26 97 The lithology at VRR appears consistent with the Murray formation mudstones analyzed
27 98 previously (Fedo et al., 2018; Heydari et al., 2018), with a grain size similarly dominated by mud
28 99 and contains occasional intervals of fine to medium sandstone, as estimated using the Mars Hand
29 100 Lens Imager on-board MSL supplemented by ChemCam LIBS data and the Gini Index Mean
30 101 Score (Edgar et al., 2020). APXS and ChemCam analyses in the Murray formation members
31 102 below and on VRR indicate that it is compositionally indistinguishable from the Murray
32 103 formation, and that Fe concentrations are not elevated for VRR; this suggests the compositional
33 104 trends from the rocks below and the rocks on VRR are largely the result of post-depositional
34 105 processes, such as diagenesis (Thompson et al., 2020; Frydenvang et al., 2020).

35 106 Rocks within the Pettegrove Point member of the ridge are thin, planar laminated, fine-
36 107 grained mudstones. Rocks within the Jura member at the top of the VRR stratigraphic succession
37 108 are also characterized by fine-grained and planar laminated facies, but with a greater degree of
38 109 variability in color (red, purple, grey and tan) and meter-scale inclined strata (Edgar et al., 2018,
39 110 2020). Generally, rocks within the Pettegrove Point member have fewer diagenetic features such
40 111 as nodules, mineral veins, fractures and erosion resistant features (L'Haridon et al., 2020), and
41 112 are lower in Al_2O_3 , SiO_2 , and higher in FeO_T than the Jura member (Thompson et al., 2020).
42 113 Both members are generally red/purple (Bennett et al., 2018) though grey bedrock patches up to
43 114 ~10 m in diameter have also been detected along VRR but are more common in the Jura member
44 115 (Frydenvang et al., 2020; L'Haridon et al., 2020). These grey patches are currently interpreted as
45 116 resulting from diagenesis, possibly from the circulation of warm, oxidizing, fluids (e.g., Bibi et
46 117 al., 2011; Peretyazhko et al., 2016, 2018; McAdam et al., 2020; Fraeman et al., 2020; Rampe et
47 118 al., 2020b) or reducing groundwater (Frydenvang et al., 2020; Horgan et al., 2020; L'Haridon et
48 119 al., 2020).

1
2
3 120 Three drill samples from VRR were analysed by the Chemistry and Mineralogy
4 121 (CheMin) instrument, which uses X-ray diffraction to determine the mineralogy of drilled
5 122 samples (Blake et al., 2012). The Stoer sample was drilled from red bedrock in the Pettegrove
6 123 Point member that contained small scale (~1 mm in diameter) concretions. The drilled samples
7 124 'Highfield' and 'Rock Hall' were acquired in the Jura Grey and Red Jura facies respectively. The
8 125 Grey Jura 'Highfield' sample was drilled at the Lake Orcadie locality, which is within a
9 126 diagenetic grey patch with abundant Ca-sulfate veins, Fe-rich nodules and dark, elongate
10 127 diagenetic features. MAHLI images before and after drilling showed that Highfield had
11 128 potentially sampled these features. The Highfield sample is also notable for the likely presence
12 129 of 'grey hematite', i.e., relatively coarse hematite with crystallites >5 μm in diameter (Rampe et
13 130 al., 2020b). On the basis of Catling and Moore's (2003) study of grey hematite, Rampe et al.
14 131 (2020b) inferred a lower temperature limit of ~100 °C for the grey hematite-bearing assemblage.
15 132 The Rock Hall Jura sample was acquired just south of the grey Lake Orcadie area in a red patch
16 133 of bedrock with an unusual, shiny, nodular appearance.

17 134 *Mineralogy of the Murray Formation*

18 135 CheMin analyzed drilled rock powders from the Murray samples Confidence Hills,
19 136 Mojave2, Telegraph Peak, Buckskin, Oudam, Marimba, Quela, Sebina, and Duluth below VRR,
20 137 and Stoer, Highfield, and Rock Hall on VRR itself (Rampe et al., 2020a). Of these drilled rock
21 138 powders, the last eight (Oudam through Rock Hall) belong to the hematite-clay mineral group
22 139 investigated in this paper. CheMin data show the presence of detrital igneous minerals and
23 140 products of aqueous alteration in these eight samples. Details of the mineralogy of these samples
24 141 are reported by Bristow et al. (2018), Rampe et al. (2020a), Achilles et al. (2020), and Rampe et
25 142 al. (2020b). All eight samples contain abundant primary magmatic minerals in the form of
26 143 plagioclase feldspar (19 – 24 wt.% of the bulk sample) with unit-cell parameters consistent with
27 144 an andesine composition and lesser amounts of pyroxene (1 – 9 wt.% of the bulk sample), alkali
28 145 feldspar (<3 wt.% of the bulk sample) and quartz (<1 wt.% of the bulk sample). The low angular
29 146 resolution of CheMin prevents a confident identification of the type(s) of pyroxene present
30 147 (Rampe et al. 2020b).

31 148 Phyllosilicates are present in every sample but vary in structure and abundance through
32 149 the stratigraphy. Ferripyrophyllite ($\text{Fe}_2\text{Si}_4\text{O}_{10}(\text{OH})_2$), a member of the talc-pyrophyllite group, is
33 150 the most likely phyllosilicate in Oudam (3 ± 1 wt.% of the bulk), based on position and breadth
34 151 of the (001) basal peak (9.6 Å in CheMin data) and the H_2O evolution profile observed from the
35 152 SAM EGA analysis (Bristow et al., 2018; Achilles et al., 2020). In Marimba, Quela, and Sebina
36 153 the phyllosilicate basal spacings and the positions of the (02l) band suggest a mix of dioctahedral
37 154 and trioctahedral smectite (e.g., Bristow et al., 2018). Smectite comprises 28 ± 3 wt.% of the
38 155 bulk of Marimba, and the (02l) peak position is consistent with a 1:2 dioctahedral:trioctahedral
39 156 weight abundance ratio, with SAM EGA data consistent with Fe-montmorillonite and Mg-
40 157 saponite (Bristow et al., 2018; Achilles et al., 2020). Dioctahedral:trioctahedral ratios for the 16
41 158 ± 2 wt.% smectite in Quela and the 19 ± 2 wt.% smectite in Sebina are 1:1 and 5:3, respectively,
42 159 based on CheMin data (Bristow et al., 2018; Achilles et al., 2020). Data from Duluth indicate the
43 160 presence of exclusively dioctahedral smectite. Analysis of CheMin data for Duluth indicates $15 \pm$
44 161 7 wt.% bulk Fe^{3+} clay, with both CheMin (Rampe et al., 2020b) and SAM EGA data (McAdam
45 162 et al., 2020) consistent with the presence of nontronite. The basal spacings in the patterns from
46 163 Stoer, Highfield, and Rock Hall are at 9.6 Å instead of the 10 Å position attributed to collapsed
47 164 smectite in previous samples (Bristow et al., 2018), indicating a collapsed smectite with a small

1
2
3 165 interlayer cation or the trioctahedral phyllosilicate ferripyrophyllite (Bristow et al., 2018; Rampe
4 166 et al., 2020b). Phyllosilicate abundances for Stoer, Highfield and Rock Hall were reported to be
5 167 10 ± 5 , 5 ± 2 and 13 ± 6 wt.% bulk, respectively (Rampe et al., 2020b). Overall, the abundance
6 168 and nature of the clay minerals in conjunction with primary magmatic minerals, allows for
7 169 testing the hypothesis that all or a significant proportion of the clay minerals were formed in situ
8 170 during post-depositional diagenesis.

9
10 171 Each drill sample contains abundant Fe-oxides and/or Fe-oxyhydroxides (Achilles et al.,
11 172 2020; Rampe et al., 2020b). Hematite ($\alpha\text{-Fe}_2\text{O}_3$) is present in every sample in abundances of ~ 3
12 173 wt.% of the bulk sample for Rock Hall up to ~ 16 wt.% of the bulk sample for Stoer. The colors
13 174 of the drill tailings in Oudam and Highfield suggest grey or specular hematite is present in these
14 175 samples. Akaganeite ($\alpha\text{-Fe}^{3+}\text{O}(\text{OH},\text{Cl})$) is more abundant than hematite in Rock Hall, and
15 176 constitutes 6 wt.% of the bulk sample. A trace amount of akaganeite is present in Stoer.
16 177 Magnetite is present in Duluth, Stoer, Highfield, and Rock Hall near the detection limit of
17 178 CheMin (Rampe et al., 2020b).

18
19
20 179 Ca-sulfate minerals are prevalent in every sample, but vary in type and abundance among
21 180 samples. Most samples have all three varieties of Ca-sulfate (anhydrite – CaSO_4 , bassanite –
22 181 $\text{CaSO}_4 \cdot 0.5\text{H}_2\text{O}$, and gypsum – $\text{CaSO}_4 \cdot 2\text{H}_2\text{O}$), with the exception of Rock Hall. Rock Hall has
23 182 the greatest abundance of Ca-sulfate of these samples, in which ~ 11 wt.% of the bulk sample is
24 183 comprised of anhydrite. Duluth has the lowest abundance of Ca-sulfate of these samples, with
25 184 ~ 1.5 wt.% anhydrite, ~ 3.5 wt.% bassanite, and gypsum is at the CheMin detection limit (~ 1
26 185 wt.%; Blake et al., 2012). Jarosite ($\text{KFe}_3(\text{SO}_4)_2(\text{OH})_6$) is present in abundances up to a few wt.%
27 186 in Marimba, Quela, Sebina, Stoer, and Rock Hall (Achilles et al., 2020; Rampe et al., 2020b).

28
29
30 187 All samples contain abundant X-ray amorphous materials, and FULLPAT analyses
31 188 indicate that opal-CT comprises a portion of the X-ray amorphous materials in the Oudam and
32 189 Highfield samples. Based on mass balance calculations using CheMin mineral abundances,
33 190 crystal chemistry using CheMin mineral abundances, crystal chemistry, and bulk APXS
34 191 measurements, the composition of the X-ray amorphous component is variably enriched in Si,
35 192 Fe, and S in these samples (Achilles et al., 2020; Rampe et al., 2020b).

36
37 193 There are several hypotheses for the variations in mudstone mineralogy such as variations
38 194 in redox within the lake during the deposition of the Murray sediments (Hurowitz et al., 2017), a
39 195 combined effect of source composition, mineral transportation and alteration (Bedford et al.,
40 196 2019), diagenetic alteration at cold to low-T hydrothermal temperatures (Achilles et al., 2020;
41 197 Frydenvang et al., 2020; McAdam et al., 2020; Thompson et al., 2020; Fraeman et al., 2013,
42 198 2016; Rampe et al. 2017), or aqueous alteration of deposited sediments by a short-lived, acidic
43 199 fluid during late diagenesis (Rampe et al., 2017). In particular, the presence and crystallinity of
44 200 akaganeite on VRR indicates alteration by warm, acidic fluids (Rampe et al., 2020b).

47 201 **METHODS**

48
49 202 Thermochemical modeling is an important tool to define reaction pathways in
50 203 environments where a fluid has interacted with a rock and changed its initial mineralogy,
51 204 especially for martian environments where observations are limited compared to more accessible
52 205 environments on Earth. On Mars, a wide range of reaction pathway problems have been studied
53 206 using a variety of thermochemical tools. On the basis of Martian meteorite and orbital data,
54 207 problems such as carbonate and acidic reactions, silicate deposition, and organic molecule

1
2
3 208 reactions have been studied and tested successfully against experimental or observational results
4 209 (Griffith & Shock, 1995, 1997; Hausrath et al., 2018; McAdam et al., 2008; Tosca et al., 2004,
5 210 2008; Varnes et al., 2003; Zolotov and Mironenko, 2007, 2016; Zolotov and Shock, 1999, 2005).
6 211 CHIM-XPT and its predecessor CHILLER have been used to study a wide range of Martian P-T
7 212 regimes, mainly for clay forming environments (Bridges and Schwenzer, 2012; Filiberto and
8 213 Schwenzer, 2013; Schwenzer and Kring, 2009, 2013; Schwenzer et al., 2012), and also
9 214 successfully tested against observational ground truth in meteorites (Bridges and Schwenzer,
10 215 2012; Melwani-Daswani et al., 2016) and in situ on Mars (Bridges et al., 2015b; Schwenzer et
11 216 al., 2016; Schieber et al., 2017). It is on this basis that CHIM-XPT was used to develop and test
12 217 the models presented here.

15 218 Thermochemical modeling has limitations, which may, for example, cause the occurrence
16 219 of phases not known to form under given pressure-temperature-composition conditions in nature.
17 220 This is due to the limits in the availability of experimentally derived thermochemical data and
18 221 the resulting extrapolation of the data application beyond the pressure-temperature range of
19 222 available data. This is taken into account through careful cross checking of results. We refer
20 223 readers to a wide range of literature (e.g., Ganguly, 2008; Holland and Powell, 1998; Kühn,
21 224 2004; Reed, 1997; Rimstidt, 2014), which will provide the theoretical backing of the technique
22 225 and further insights into problem solving and decision making to limit the impact of modelling
23 226 limitations. This is especially the case for clay minerals due to limitations in the dataset in
24 227 modeling iron-bearing environments on Mars (Catalano, 2013; Chevrier et al., 2007). Therefore,
25 228 in this paper, care was taken to use all information available to constrain the modeling
26 229 parameters when evaluating the results. It is important to note that in a sedimentary environment,
27 230 or any dynamic geologic environment, the models describe reaction pathways of local
28 231 equilibrium and not an overall equilibrium of the entire geologic unit (Kühn, 2004). Thus, such
29 232 models enable the assessment of a reaction pathway for a given overall chemistry to reach the
30 233 resulting alteration assemblage.

34 234 **Thermochemical code and database**

36 235 CHIM-XPT (Reed et al., 2010) is a program for computing multicomponent
37 236 heterogeneous chemical equilibria in aqueous-mineral-gas systems and was chosen because of its
38 237 heritage in modeling basaltic and ultramafic systems (e.g., Reed, 1983; Palandri and Reed,
39 238 2004), and modeling alteration on Mars (Schwenzer and Kring, 2009; Bridges and Schwenzer,
40 239 2012; Schwenzer et al., 2012; Filiberto and Schwenzer, 2013; Bridges et al., 2015b; Schwenzer
41 240 et al., 2016; Melwani-Daswani et al., 2016; Schieber et al., 2017). The model calculation
42 241 proceeds in steps of reactant rock added to the fluid, where each step calculates equilibrium
43 242 between the fluid and the dissolved rock, meaning that each step can be treated and interpreted
44 243 independently to the direction from which it was reached, and each step determines the
45 244 properties of the minimum Gibbs free energy of the system. Step size may vary depending on
46 245 task requirements. A weight ratio of the total number of fluid grams relative to the total number
47 246 of grams of reactant rock is used, so model calculations are independent of the size of the
48 247 system, but the calculations are usually based on 1 kg (55.5 mol) of water. Precipitates are not
49 248 fractionated from the system unless stated otherwise. In CHIM-XPT, the water to rock ratio
50 249 (W/R) is the ratio of incoming fluid to reacted host rock. Inputs required for the execution of
51 250 CHIM-XPT in this study were the starting fluid composition, reactant rock chemical
52 251 composition, system temperature and pressure. We assume that the diagenesis was disconnected
53 252 from the atmosphere, as can be expected from a subsurface fluid. Therefore, we did not include a

1
2
3 253 gas phase at the start of the calculations and did not replenish any CO₂ or other components
4 254 typically found in the Martian atmosphere. We note that gas phases were allowed to form, should
5 255 they have become stable, but none were observed at the conditions that led to clay and hematite
6 256 formation.

8 257 The SOLTHERM thermodynamic database used with CHIM-XPT in this study contains
9 258 the following sheet silicates: talc (Mg, Fe, Mg-Al endmembers); pyrophyllite; chlorites
10 259 (clinochlore, daphnite, Mn-chlorite, Al-free chlorite); kaolinite; illite; montmorillonite (Ca, K,
11 260 Mg, Na endmembers); beidellite (Ca, H, K, Mg, Na endmembers); nontronite (Ca-, H-, K-, Mg-,
12 261 Na-nontronite); serpentine (antigorite, chrysotile, greenalite); sepiolite. The only member of the
13 262 kaolinite group the database contains is kaolinite. There is no saponite or vermiculite in the
14 263 database, which may affect the results and therefore comparisons between our modeled mineral
15 264 assemblages and the observed mineral assemblages on Mars. In this study, results are plotted in
16 265 mineral abundance (wt.%) vs W/R, with chlorite endmembers (Fe²⁺ sheet silicate and nontronite
17 266 endmembers (Fe³⁺ clay mineral) combined. Given the limitations of the thermochemical
18 267 database with regards to the full range of possible phyllosilicates, in this study the modeled
19 268 phyllosilicate assemblages are summed to calculate an average clay mineral with average
20 269 composition that is then taken as a chemical analogue to the clay minerals observed in Gale
21 270 crater. As discussed in discussion section "Clay minerals and comparisons to Yellowknife Bay
22 271 and other Martian terrains, including Nakhilite Martian Meteorites", this is consistent with
23 272 previous approaches by Bridges et al. (2015b) and Schwenzer et al. (2016).

27 273 Critical evaluation of the results and comparison to terrestrial mineralogy are required to
28 274 further evaluate the modeling results. Extrapolation of the thermodynamic data from higher
29 275 temperature might occur in the low temperature range modeled here, which can lead to the
30 276 occurrence of mineral phases not known to form at the given pressure-temperature range. This
31 277 problem is dealt with through careful evaluation of every phase forming and exclusion of those
32 278 known to not form in the given pressure-temperature range, owing to kinetic constraints at low
33 279 temperature (Melwani-Daswani et al., 2016, supporting material). The temperature transition
34 280 between the Fe-oxides, goethite and hematite, was taken into consideration for the modeling. As
35 281 documented by Cornell and Schwertmann (2006; and references therein) fine grained goethite is
36 282 stable ≤ 25 °C, relative to coarse grained hematite. However, in laboratory environments where
37 283 ferrihydrite was stored as aqueous suspensions at 24 °C and pH between 2.5 and 12, both
38 284 hematite and goethite form, with the highest hematite abundance forming between pH 7 and 8
39 285 and the highest abundance of goethite forming at pH 4 and pH 12 (Schwertmann and Murad,
40 286 1983). The formation of other Fe-oxides such as ferrihydrite, goethite and akaganeite may have
41 287 occurred first in the sediments of Gale crater and later transformed to hematite via mechanisms
42 288 documented by Cornell and Schwertmann (2006; and references therein). However, while those
43 289 precursors could have been a factor in some of the rocks we are studying, such as those that had
44 290 high amounts of Fe in their amorphous components, it is difficult to definitively identify poorly
45 291 ordered/amorphous Fe phases such as ferrihydrite with *Curiosity's* payload, and at the time of
46 292 writing there is no direct evidence for ferrihydrite. For the purposes of this modeling study we
47 293 assume direct precipitation of goethite or hematite from the modeled porewater-rock interactions,
48 294 and not from the alteration of ferrihydrite. Magnetite was allowed to form but did not under the
49 295 conditions modeled here at the W/R assumed relevant.

54 296 A list of the minerals excluded in each model can be found in the supplementary material
55 297 (Table S3). The model calculations show finer details than any of the sources of information

1
2
3 298 from Mars: detection limit for the phase abundances with CheMin on *Curiosity* is ~1 wt.%
4 299 (Blake et al., 2012) and the pixel footprint of CRISM is nominally 18 m, (Murchie et al., 2007)
5 300 limiting the detection of trace phases in both instances. Therefore, small proportions of a mineral
6 301 phase (<5 wt.%) within a modeled alteration assemblage may not be easily comparable to the
7 302 observed martian mineralogy. Minerals modeled to form that have not been observed in the
8 303 Murray formation, either in-situ with *Curiosity* or remotely with CRISM, were allowed to form
9 304 due to a lack of justification for their removal.

305 **Modeled water-rock ratio**

306 CHIM-XPT thermochemically calculated mineral assemblages are illustrated as plots of
307 mineral abundance (weight %) vs W/R ratio (e.g. Fig. 5 – 7). W/R ratio is a progress variable
308 which indicates limited reactant rock dissolution at high W/R with a relative increase in reactant
309 rock dissolution at low W/R. The mass of alteration minerals precipitated ranges from 0.01 g at
310 100,000 W/R to 1,000 g at 1 W/R. CHIM-XPT works on the basis of complete dissolution of the
311 defined reactant rock components in relevant W/R proportions per interaction step. While in real-
312 world systems only partial host rock dissolution occurs (making the W/R values reported here
313 comparably higher), modeling complete host rock dissolution enables a systematic investigation
314 of modeled alteration minerals and associated fluids as a function of the W/R process variable.
315 High W/R (>5,000) is representative of a system where only a small amount of the rock is
316 dissolved in a large mass of fluid (i.e., where only a limited surface area interacts with the fluid
317 and/or timescales are short). This can represent freshwater inflow environments such as in rock
318 fractures or rock surfaces exposed to regular precipitation. Lower W/R ranges are more
319 representative of minimal fresh-fluid inflow and stagnant fluids reacting with large rock surfaces.
320 Comparison to experiments and geologic analogs show that W/R of around 1,000 is generally
321 representative of water-rich diagenetic or small fracture settings, whereas lower W/R are
322 comparable to low-water diagenetic and eventually metamorphic conditions. For an in-depth
323 discussion how model and experimental water to rock ratios compare, see Olsson-Francis et al.
324 (2017). CHIM-XPT calculates the equilibrium reaction of the fluid with the precipitating phases
325 at an overall chemistry of the system.

326 **HYPOTHESIS AND MODEL SET-UP**

327 The purpose of this study is to constrain the formation conditions (W/R, temperature,
328 redox, pH) under which the hematite-clay mineral assemblages observed on and below VRR
329 precipitated. More specifically, we test the hypothesis that the formation of clays and hematite in
330 the Murray formation on and below VRR is of groundwater type, which stands in a continuation
331 of previous studies. For Yellowknife Bay, the lowest point in the stratigraphy encountered by
332 *Curiosity* early in the mission, studies showed that groundwater-type, circumneutral fluids could
333 explain the clay mineral formation with sulfate formation representing a distinct, later alteration
334 event (Bridges et al., 2015b; Schwenzer et al., 2016). Hausrath et al. (2018) came to a similar
335 conclusion for Stimson formation alteration, where early was dominated by olivine- in
336 circumneutral fluids and no redox-change was required to explain the observations. In this study,
337 however, we focus on the alteration of a magmatic host rock chemistry, as could be deposited by
338 the fluvial-lacustrine conditions described for Gale crater, in a circumneutral groundwater.

339 There is a wide range of fluid-related observations and phenomena observed before the
340 *Curiosity* rover encountered VRR, such as overall lake water changes (Hurowitz et al., 2017),

1
2
3 341 nodules (Nachon et al., 2014) and silica-rich haloes (Frydenvang et al., 2017), some of which are
4 342 also observed on VRR. Other studies of VRR alteration (Fraeman et al., 2020; L'Haridon et al.,
5 343 2020; McAdam et al., 2020; Rampe et al., 2020b; Yen et al., 2020) assume a multi-stage fluid
6 344 evolution or a diversity of fluids to explain their observations. This leads to testing the
7 345 hypothesis in this paper that the first step of alteration was one of in situ diagenesis in a dilute,
8 346 circumneutral fluid. This study is in context of the late-stage phases (Ca-sulfate, jarosite,
9 347 akaganeite) forming when fluid concentrations had evolved to higher sulfate concentration, or
10 348 more generally higher salinity, and locally to acidic conditions (Achilles et al., 2020; L'Haridon
11 349 et al., 2020; McAdam et al., 2020; Rampe et al., 2020b; Yen et al., 2020). This is further
12 350 supported by SAM investigations of jarosite-bearing sediments showed a bimodal age
13 351 distribution with a much younger potential formation age for the jarosite-bearing alteration
14 352 (Martin et al., 2017). Therefore, modeling the reaction pathways of the late-stage Ca-sulfate,
15 353 jarosite, and akaganeite is not a goal of this study.

19 354 **The starting fluid**

20
21 355 Gale Portage Water (GPW) (Bridges et al., 2015a, 2015b; Schwenzer et al., 2016; Turner
22 356 et al., 2019) was used as the fluid in this study, making results presented here for the Murray
23 357 formation directly comparable to the studies for Yellowknife Bay. This fluid was derived from
24 358 equilibration of a fluid used previously in Mars fluid-rock interaction modeling (Schwenzer and
25 359 Kring, 2009) with the basaltic Portage Soil composition sampled from the Rocknest aeolian
26 360 bedform in Gale crater (Bish et al., 2013). As argued in Bridges et al. (2015b), this assumed that
27 361 Rocknest can be regarded as an average crustal composition in Gale crater, and GPW is a fluid of
28 362 groundwater-type concentration directly derived from local bedrock. Because of the dilute nature
29 363 of this fluid, the chemistry of the rock reactants becomes the dominating factor in the water-rock
30 364 reaction modeling. Thus, providing additional confidence that reaction pathways described here
31 365 are directly applicable to *Curiosity's* observations in the Murray Formation. The exact W/R at
32 366 which the rock composition dominates the reaction is dependent on the solubility of the element
33 367 considered and its concentration in the rock. Influence of the fluid is highest for elements not
34 368 contained in the rock, which mostly concerns volatiles such as CO₂. However, CO₂ concentration
35 369 is low (1.68×10^{-4} mole/L) and does not typically lead to the formation of carbonates beyond
36 370 trace level. A detailed summary of how this fluid was derived is given in Bridges et al (2015b),
37 371 and the fluid composition is given in Table 3 of Bridges et al. (2015b). Chlorine concentration in
38 372 GPW is about an order of magnitude higher than CO₂, at 5.76×10^{-3} mole/L, but chlorine does
39 373 not participate in mineral formation. It is an important carrier of ionic strength at the very highest
40 374 W/R, but at the W/R considered important here, does not cause any change of the system. It also
41 375 is a potential complexing anion to increase Fe-solubility (e.g., Cornell and Schwertmann, 2006),
42 376 but Cl concentrations are too low to significantly increase Fe-concentration in the fluid (Bridges
43 377 et al., 2015b). Our Fe-concentrations are generally in family with other similar models (e.g.,
44 378 Marion et al., 2003). Cl-concentrations only influence apatite formation, which forms as Cl-
45 379 apatite instead of hydroxyl-apatite, if Cl-concentrations are significant, but forms F-apatite once
46 380 fluorine is present (Filiberto and Schwenzer, 2013). We note that – due to the lack of quantitative
47 381 fluorine data for VRR rocks – we have not incorporated fluorine into the system. The solution is
48 382 initially oxidizing with all S species as SO₄²⁻, and the redox in the fluid is controlled by the SO₄²⁻/
49 383 /HS⁻ pair. The redox of the system throughout each model is dependent on the Fe²⁺/Fe³⁺ ratio of
50 384 the total Fe in the reactant rock composition. The fluid composition is represented in each

1
2
3 385 calculated step by a set of 112 different ionic species. Unless stated otherwise, fluid pH was
4 386 modeled as a free parameter.

6 387 **Host rock composition**

8 388 The *Curiosity* samples studied are mixtures of primary magmatic phases, such as
9 389 pyroxene and plagioclase (Achilles et al., 2020; Rampe et al., 2020b), and alteration phases such
10 390 as phyllosilicates and hematite (Rampe et al., 2020b; McAdam et al., 2020). Olivine is absent in
11 391 the samples, which is in agreement with literature sources that have shown it to be the first
12 392 mineral to dissolve in water-rock reactions (e.g., Gudbrandson et al., 2011; Hausrath et al.,
13 393 2018). To use chemistry and mineralogy data from *Curiosity* to isochemically model the
14 394 diagenetic alteration assemblage that occurred in the Murray formation, the unaltered host rock
15 395 component needs to be removed from the model input data. For this, the chemistry of the
16 396 observed alteration must be considered. Hereby defined in this study as “chemical alteration
17 397 compositions”, the chemistry of the altered components was calculated and used as the reactant
18 398 host rock composition in the thermochemical modeling as follows:

21 399 Calculating the chemical alteration compositions was undertaken by combining
22 400 measurements taken by APXS and CheMin instruments on-board the *Curiosity* rover for drilled
23 401 samples obtained in the Murray formation: Oudam, Marimba, Quela, Sebina, Duluth, Stoer,
24 402 Highfield and Rock Hall (summarized in introduction section “Overview of the Murray
25 403 formation”). Using crystal chemistries derived for the magmatic minerals (Table S1) (Morrison
26 404 et al., 2018; Achilles et al., 2020; Rampe et al., 2020b) and their abundances determined using
27 405 CheMin data (Bristow et al., 2018; Rampe et al., 2020a), the associated compositional oxide
28 406 wt.% contributions were subtracted from the bulk APXS measurements. Ca-sulfates observed by
29 407 CheMin (Achilles et al., 2020; Rampe et al., 2020b) were also removed as these have been
30 408 shown to have formed during late diagenesis (Nachon et al., 2014), during a possible two-step
31 409 process (Schwenzer et al., 2016). This approach includes contributions from the amorphous
32 410 component that, at the time of writing, is not well understood and is hypothesized to contain
33 411 primary basaltic glass, nanophase Fe-oxides, amorphous sulfates, and sulfides (Bish et al., 2013;
34 412 Smith et al., 2019; Rapin et al., 2019; Rampe et al., 2020a; Achilles et al., 2020; Wong et al.,
35 413 2020). The approach taken here, to input the chemical composition of the host rock and not the
36 414 mineral composition, raises questions as to what was the phase composition and abundances
37 415 within the host rock. In discussion section “Comparison of modeled mineral phases with Murray
38 416 Formation observations” we use comparisons between the modeled data in this paper and the
39 417 observations made by *Curiosity* to infer compositional characteristics regarding the amorphous
40 418 phase identified observed in Gale crater, including the possibility of a volcanic glassy
41 419 component.

42 420 Given the young, Amazonian age inferred from K-Ar investigations of the jarosite in the
43 421 Mojave drill sample (Martin et al., 2017), it is also assumed that the observed akaganeite and
44 422 jarosite formed during late-stage acidic alteration after the formation of hematite and clay
45 423 minerals (e.g. Achilles et al., 2020; Rampe et al., 2020b). Thus, the formation of akaganeite and
46 424 jarosite is not within the scope of this study. However, their chemical composition is included in
47 425 the calculated alteration composition as their formation is likely the result of localized alteration
48 426 where elements were remobilized from the products of the first step of diagenesis that is being
49 427 modeled here.

428 **Pressure-Temperature space**

429 The temperatures selected for modeling were 25 °C, 50 °C, 75 °C and 100 °C, as this
430 broad range can be consistent with the alteration mineralogy observed in Gale crater (Bristow et
431 al., 2018; Rampe et al., 2020a). The pressure was selected to prevent boiling for each
432 temperature. Results were then evaluated with respect to temperature and used as a guide for
433 thermochemical modeling where reactant rock was the calculated chemical alteration
434 compositions for drill samples collected in the Murray formation below VRR and the overall
435 Murray formation.

436 **Redox considerations**

437 No direct measurements of overall redox conditions in the rock were possible (e.g.,
438 because of the presence of the amorphous phase; Achilles et al., 2020; Rampe et al., 2020b).
439 Thus, different $\text{Fe}^{2+}/\text{Fe}^{3+}$ ratios were modeled. Resultant modeled mineral assemblages were then
440 compared to assemblages observed by *Curiosity* to evaluate the plausibility of the model. Models
441 were run at host rock chemistries of 0.1 and 0.5 $\text{Fe}^{3+}/\text{Fe}_{\text{tot}}$ to explore the varying effect on the
442 resultant alteration mineral assemblage. SO_3 was recalculated as FeS and the equivalent amount
443 of Fe was subtracted from FeO. Cl was recalculated as NaCl and the equivalent amount of Na
444 was subtracted from Na_2O .

445 **MODEL RESULTS**

446 **Calculation of the host rock composition**

447 The result of the magmatic mineral subtraction process (hypothesis and model set-up
448 section “Host rock composition”) shows a similar chemical alteration composition throughout
449 the Murray formation below VRR (Fig. 3). SiO_2 varies between 45 and 49 wt.% (Fig. 3), FeO_T
450 has a larger variation, between 23 and 29 wt.%, and a positive correlation with SiO_2 . MgO varies
451 between 5 and 7 wt.%, Al_2O_3 between 5 and 7 wt.%. Alkali oxides (Na_2O and K_2O) are below 2
452 wt.% in all calculated alteration compositions below VRR. The three samples acquired on VRR
453 display a larger variability in SiO_2 , varying from 35 to 54 wt.%. FeO_T has a similar variation to
454 below VRR, varying between 23 and 29 wt.%. MgO is also similar in range on VRR compared
455 to below, 3 to 6 wt.%, while Al_2O_3 is lower on VRR, ranging from 3 to 6 wt.%. Alkali oxides
456 (Na_2O and K_2O) are below 2 wt.% in all calculated chemical alteration compositions on VRR.

457 For the VRR samples, there are some noteworthy observations for the chemical alteration
458 compositions (Fig. 3): The Rock Hall and Highfield drill holes sampled red and grey Jura,
459 respectively, with the FeO_T in our calculation being about 5% higher in Rock Hall than in
460 Highfield. The red Jura target, Rock Hall, is very similar in FeO_T to the red Pettegrove Point
461 Stoer target. When averaged over the entirety of the drilled samples, chemical alteration
462 compositions below and on VRR are remarkably similar (Fig. 4), pointing towards local element
463 mobility. This confirms that the fluid influence is minimal, and supports our assumption of a
464 dilute incoming fluid, but also points towards the absence of a large-scale fluid movement in
465 late-stage diagenesis after the formation of the hematite-clay dominant mineral assemblage.

466 The proportion of alteration minerals of the different samples was also assessed, with the
467 ratio of alteration to primary mineral content detailed in Table 1. These ratios indicate that, if Ca-
468 sulfates are excluded, samples below VRR contain a greater fraction of identified alteration
469 products compared to VRR, with Duluth containing the least amount of alteration. This is

1
2
3 470 consistent with Mangold et al. (2019a; 2019b) who showed a decrease in the Chemical Index of
4 471 Alteration above the Sutton Island member. We have thus decided to model the average
5 472 alteration composition of VRR and compare those models to models which use an overall
6 473 average alteration composition and an average alteration composition for below VRR (excluding
7 474 Duluth as this had further diagenetic features). A comparison of the mean alteration chemical
8 475 compositions for the pre-VRR Murray formation (Oudam to Sebina) and for VRR Murray (Stoer
9 476 to Rock Hall) shows that they are similar (Fig. 4, see also Table S4) with the standard deviation
10 477 of these mean compositions overlapping.

13 478 **Alteration mineralogy in a groundwater-dominated setting**

14
15 479 As described above, we hypothesize that the sediments in the Murray formation on and
16 480 below VRR were altered in situ from magmatic detrital precursors, and our model with the
17 481 calculated chemical alteration composition described above then allows us to compare a
18 482 predicted mineral assemblage with what has been observed by *Curiosity*. The reasoning for this
19 483 is that what currently remains as unaltered phases will not have taken part in the reactions, and
20 484 what is now the alteration assemblage was once a magmatic mineral, e.g., olivine, pyroxene,
21 485 plagioclase, and has been reacted into the minerals we find now. With this composition we
22 486 modeled the average VRR Murray alteration composition isothermally at four different
23 487 temperatures. The resulting mineral assemblages can be divided into three W/R sections. At very
24 488 high W/R (above W/R of 10,000), models between 50 and 100 °C show a hematite-clay mineral
25 489 assemblage whereby the dominant clay is chlorite (Fig. 5 and 6). At 25 °C, goethite forms
26 490 instead of hematite (Fig. 5A and 6A). Between W/R of 10,000 and 100, nontronite dominates;
27 491 below W/R of about 100 a talc-chlorite assemblage forms. This generalized pattern applies for
28 492 different redox settings as well as for the VRR-only and ‘all Murray’ compositions (Fig. 5 – 7).

29
30 493 Assessing the influence on temperature in the system that has 10% of the FeO_T as Fe^{3+}
31 494 (Fig. 5A-D) shows that the W/R range in which nontronite forms becomes smaller and the
32 495 amount of nontronite forming decreases as the temperature increases from 25 °C to 100 °C.
33 496 Instead of nontronite, a hematite–chlorite assemblage forms at high W/R. Note also the increased
34 497 abundance of SiO_2 with increasing temperature. At low W/R, changes are limited to small
35 498 compositional changes, leading to the formation of a few wt.% of epidote at the highest
36 499 temperature. This metamorphic assemblage is not found at Gale crater, for which reason we
37 500 focus the discussion in the next section on the high and intermediate W/R.

38
39 501 In the more oxidizing system (50% of the FeO_T as Fe^{3+} ; Fig. 6A-D), changes are subtle.
40 502 Thermochemical models run at 25 °C show goethite abundances vary from 7.5 wt.%, 2.0 wt.%
41 503 and 0.0 wt.% for models with 10% $\text{Fe}^{3+}/\text{Fe}_{\text{tot}}$ to 9.6 wt.%, 1.6 wt.% and 5.2 wt.% for models with
42 504 50% $\text{Fe}^{3+}/\text{Fe}_{\text{tot}}$, at 10,000 W/R, 1,000 W/R and 100 W/R, respectively. At and above 50 °C,
43 505 hematite forms instead of goethite. As expected, hematite content increases with increasing Fe^{3+}
44 506 availability, meanwhile Fe-sulfide decreases (Tables S5 and S6).

45
46 507 The nontronite field expands towards intermediate and lower W/R, and so does that of
47 508 the SiO_2 -phase, which forms around W/R of 1,000 – 10,000 (Fig. 5 and 6, Table S7). We note,
48 509 though, that the overall pattern of a hematite-clay mineral assemblage at high W/R and
49 510 nontronite at intermediate W/R remains stable (Table 2). However, at high W/R the dominant
50 511 clays are chlorites, the onset of which occurs at lower W/R with increasing temperature (Fig. 5
51 512 and 6). Modeling the different Murray averages (Table S4) at 50 °C and at 10% and 50% FeO_T
52 513 as Fe^{3+} returns almost indistinguishable results (Fig. 7), which demonstrates that the hematite-

1
2
3 514 clay mineral assemblage is the dominant assemblage at high water to rock ratios over a wide
4 515 range of environmental conditions.

6 516 **Summary of the modeled alteration mineral assemblages**

8 517 Thermochemical modeling undertaken for this study has focused on the hematite-clay
9 518 mineral alteration assemblage observed in the Murray formation, with emphasis on sedimentary
10 519 rocks on and below VRR. Chemical compositions of the alteration mineral assemblages
11 520 observed by *Curiosity* were calculated and used as the reactant rock chemical compositions for
12 521 thermochemical modeling. Modeled alteration mineral assemblages have been produced for a
13 522 variety of W/R, temperatures and varying $\text{Fe}^{3+}/\text{Fe}_{\text{tot}}$ content (Fig. 5 and 6).

15 523 For the models in this study, at and above 50 °C hematite forms, which is likely a result
16 524 of its higher thermodynamic stability compared to goethite (Cornell and Schwertmann, 2006 *and*
17 525 *references therein*) and makes these models directly comparable to observations by *Curiosity*.
18 526 Table S5 gives details of the modeled hematite abundances showing an increase in hematite
19 527 abundance with temperature at 10,000 and 1,000 W/R, with an additional increase associated
20 528 with Fe^{3+} availability. Magnetite was allowed to form in the models (Fig. 5 and 6) but did not
21 529 form at the W/R assumed relevant. Table S6 demonstrates that Fe-sulfide abundance increases
22 530 with temperature at 10,000 W/R with minor wt.% variation at 1,000 W/R and 100 W/R. Fe-
23 531 sulfide abundances decrease at all W/R with increased Fe^{3+} availability.

26 532 The dominant clay minerals, when formed in our thermochemical models, belong to the
27 533 smectite group (nontronite), though in some cases significant chlorites form. Clay mineral
28 534 abundance varies significantly with temperature. In summary, the overall clay abundance
29 535 decreases with temperature regardless of Fe^{3+} availability (Table S8); however, there is an
30 536 increase in clay abundance at 1,000 W/R and 100 W/R from 10% $\text{Fe}^{3+}/\text{Fe}_{\text{tot}}$ to 50% $\text{Fe}^{3+}/\text{Fe}_{\text{tot}}$ at
31 537 each modeled temperature. Summed in Table S7, there is a clear decrease in nontronite
32 538 abundance with temperature and a significant increase at 100 W/R with increased Fe^{3+}
33 539 availability. The chlorite abundance increases with temperature and decreases with Fe^{2+}
34 540 availability (Table S9). The third group of clay minerals that formed in the models in this study
35 541 was talc; for each modeled temperature, talc forms with increasing abundance from 10,000 – 1
36 542 W/R (Fig. 5 and 6). Overall, talc abundance decreases with temperature and Fe^{2+} availability
37 543 (Table S10).

40 544 Thermochemical modeling at 50 °C for the calculated alteration chemical compositions
41 545 for the rocks below VRR and the overall Murray formation (Fig. 7) returned near
42 546 indistinguishable results at high W/R compared to the calculated chemical alteration composition
43 547 for the rocks on VRR (Fig. 5 and 6). This implies dominance of a hematite-clay mineral
44 548 assemblage for high W/R over a range of environmental conditions.

47 549 To assess redox, all Fe- and S-bearing phases have to be taken into account. We note here
48 550 that ferrous (including magnetite) and ferric minerals form at different W/R. The main influence
49 551 on redox is expected from variations in the host rock chemical composition, especially in a
50 552 subsurface system without access to atmospheric CO_2 . While, as stated in the results section, the
51 553 main silicate mineral composition remains largely unaffected by redox, there are differences in
52 554 the hematite/sulfide ratio (Fig. 5 and 6). Taking 75 °C as an example (Tables S5 and S6), 9.6
53 555 wt.% hematite and 10 wt.% pyrite precipitate from the system at 1,000 W/R and 10% Fe_{tot} as
54 556 Fe^{3+} . In contrast, at 50% Fe_{tot} as Fe^{3+} in the host rock, the hematite/sulfide ratio increases from

1
2
3 557 approximately 1 to 1.4 (12 wt.% hematite and 8.5 wt.% pyrite). However, at lower temperatures,
4 558 and higher and lower W/R, the situation is different.

5
6 559 The pH for the models shown in this paper (Fig. 5 and 6) at 10,000 W/R ranges from 7.9
7 560 to 9.3, as shown in Fig. 8. At 10,000 W/R for the VRR Murray composition derived in Table S4,
8 561 the pH trends from 9.4 to 8.0 for 25 to 100 °C at 10% Fe³⁺/Fe_{tot} content and 9.2 to 7.9 for 25 to
9 562 100 °C at 50% Fe³⁺/Fe_{tot} content. For pre-VRR Murray and overall Murray compositions in
10 563 Table S4, the pH is 8.8 for 10% Fe³⁺/Fe_{tot} content and the pH is 8.7 for 50% Fe³⁺/Fe_{tot}. We
11 564 attribute this increase in pH with decreasing W/R to H being consumed by phyllosilicate
12 565 formation as increasing pH is commonly observed with decreasing W/R and increasing
13 566 phyllosilicate formation (e.g., Schwenger and Kring 2009, Bridges and Schwenger, 2012;
14 567 Bridges et al., 2015b).

17 568 DISCUSSION

18
19 569 Our discussion first assesses the modeled mineral assemblages in context with the
20 570 observations of the Murray formation. We then compare to other Martian-based models before
21 571 looking at terrestrial comparisons.

23 572 Comparison of modeled mineral phases with Murray Formation observations

24
25 573 The modeled early diagenetic mineral assemblages (Fig. 5 – 7) were compared to mineral
26 574 phases observed by CheMin. To compare the modeled clay minerals to observations in the
27 575 Murray formation, their chemistry is considered in discussion section “Clay minerals and
28 576 comparisons to Yellowknife Bay and other Martian terrains, including the Nakhilite Martian
29 577 Meteorites”. Whilst the modeling method used in this study calculates chemical equilibrium at
30 578 specific W/R, it is important to remember that low-temperature diagenetic processes are
31 579 dominated by chemical kinetics (Misra, 2012). For this reason, we rely on comparisons with the
32 580 ground truth – the observed mineralogy at VRR – for the setup of our model and the
33 581 interpretation of our results. It is the combination of ground truth from the rover instruments with
34 582 the models that allow us to arrive at our conclusions.

35
36
37 583 The abundances of Fe-oxides formed in the models varies with Fe³⁺/Fe_{tot} content and,
38 584 depending on temperature, speciation. Thermochemical models run at 25 °C do not compare well
39 585 with *Curiosity* observations with regards to Fe-oxide abundance with clay (Tables 2 and 4), and
40 586 as hematite, not goethite, is observed in the drilled samples (Achilles et al., 2020; Rampe et al.,
41 587 2020b). As goethite can transform to hematite over time (Cornell and Schwertmann, 2006 *and*
42 588 *references therein*) there is a possibility that these lower temperature models reflect the actual
43 589 reaction pathway, and that the hematite-clay mineral assemblage observed in the Murray
44 590 transformed from a goethite-clay mineral assemblage with burial and diagenesis of the
45 591 sediments. It is important to note that, like goethite, ferrihydrite or magnetite could have also
46 592 been precursors to the hematite observed in the Murray formation. This possibility is discussed
47 593 by Achilles et al. (2020) for the hematite observed in Oudam and by Rampe et al. (2020b) for the
48 594 samples on VRR. The mechanisms to transform ferrihydrite to hematite include aqueous
49 595 suspension under weakly acidic to weakly alkaline pH, and aging in a humid environment
50 596 (Cornell and Schwertmann, 2006 *and references therein*). These mechanisms are discussed by
51 597 Rampe et al. (2020b) for VRR with particular note on hematite crystallite size being an indicator
52 598 for formation process. Magnetite was observed by *Curiosity* on VRR in Duluth, Stoer and
53 599 Highfield (Rampe et al., 2020b), and is also a potential precursor that can be transformed to

1
2
3 600 hematite by oxidation. Magnetite was included in the chemical alteration compositions.
4 601 Therefore, the models do not rule out the transformation of other Fe-oxides to hematite.
5 602 However, in this study it is assumed that the present-day Fe-oxides observed in the Murray
6 603 formation and VRR are what precipitated at the time of formation and have not since
7 604 transformed, and so the thermochemical modeling results are compared to *Curiosity*
8 605 observations.

9
10 606 Ca-sulfate veining has been observed extensively in Gale crater (introduction section)
11 607 and their removal from the compositional data prior to modeling complicates the identification of
12 608 Ca-rich phases in our models. In addition, trace amounts of carbonates such as calcite and
13 609 rhodochrosite have not been observed with CheMin in the samples in this paper at the time of
14 610 writing (January 2021). For these reasons, trace amounts of calcite, rhodochrosite, merwinite
15 611 ($\text{Ca}_3\text{MgSi}_2\text{O}_8$) and spurrite ($\text{Ca}_5\text{Si}_2\text{O}_8(\text{CO}_3)$) were excluded from the thermochemical model
16 612 plots (Fig. 5 – 7). However, siderite may be present in Rock Hall (Rampe et al., 2020b), and
17 613 Fe/Mg/Fe-Mg carbonates have been identified in SAM EGA data of samples from the Stimson
18 614 formation (Sutter et al., 2017). It has been suggested, using an experimental approach on martian
19 615 crust simulants, that carbonates only form when olivine is abundant and would not form in
20 616 olivine-free assemblages under a CO_2 atmosphere (Baron et al., 2019).

21
22
23 617 The hematite/sulfide ratio is mainly controlled by the variation in the onset of nontronite
24 618 formation (at systematically lower W/R with increasing temperature) under high-W/R
25 619 conditions, and at low-W/R by the ratio of nontronite to celadonite as Fe-phyllsilicate phase.
26 620 This demonstrates that the main redox sensitivity of such systems might not be discernible via
27 621 the clay minerals alone. Phyllosilicates and their role in interpretation of the Mars samples is still
28 622 being refined (Hurowitz et al., 2017; Bristow et al., 2018) and models suffer from uncertainties
29 623 in the thermochemical data for these minerals (Catalano, 2013). Thus, it is encouraging to see
30 624 that the system changes within strictly constrained boundaries of the input redox parameter
31 625 conditions of the host rock.

32 33 34 35 626 **Comparison of modeled mineral abundances to the observed Murray Formation** 36 627 **mineralogy**

37
38 628 For comparing the modeled mineral assemblages in this paper to observations made by
39 629 *Curiosity*, we also considered the relative abundance of the observed altered phases. The
40 630 observed CheMin clay mineral / Fe-oxide ratios in Table 4 are most comparable with the
41 631 modeled ratios at 50 °C and 10,000 W/R shown in Tables 2 and 3, as also shown in Fig. 9. Fig. 9
42 632 shows that the observed CheMin ratios are not comparable with modeled clay mineral / Fe-oxide
43 633 ratios at 50 °C for 1,000 or 100 W/R. Summing all Fe-oxides reported by CheMin significantly
44 634 lowers the clay mineral / Fe-oxide ratio for VRR (Table 4), largely due to akaganeite in the Rock
45 635 Hall drilled sample. As previously discussed, akaganeite might belong to a later alteration phase
46 636 and formed independent of the hematite-clay mineral diagenetic environment where Fe is
47 637 remobilized. To quantitatively compare the modeled and observed alteration mineral
48 638 assemblages, we have plotted hematite content vs clay mineral content from *Curiosity* drill
49 639 samples and from our thermochemical models at 10,000 W/R (Fig. 10). In Fig. 10, CheMin
50 640 abundances of clay minerals and hematite are normalized to the calculated alteration component,
51 641 which includes the composition of the amorphous component. The samples analysed by CheMin
52 642 show a trend, whereby samples with high clay content are generally lower in hematite. The
53 643 modeled alteration assemblages also show this trend with high clay content corresponding to low
54
55
56
57
58
59
60

1
2
3 644 hematite abundances in the modeled alteration assemblage. Thus, the models and samples show
4 645 the same correlation between hematite and clays, although the concentration of both is generally
5 646 higher in the modeled alteration phase compared to the drilled samples. In Fig. 10, the linear
6 647 trend of clay mineral and hematite abundances at 10,000 W/R from our thermochemical models
7 648 at 50 °C is parallel to the trend for CheMin samples Marimba, Sebina, Quela, Highfield and
8 649 Oudam. Linear regression analysis revealed the comparability of these trends, with a gradient -
9 650 2.35 ± 0.09 for the thermochemical models run at 50 °C and -1.88 ± 0.56 for Oudam, Marimba,
10 651 Sebina, Quela, Duluth, Highfield and Rock Hall, with respective R^2 values of 0.99 and 0.70. The
11 652 uncertainty associated with Duluth clay mineral and hematite abundance is within this negative
12 653 correlation, so was included in the regression analyses. Rock Hall does not clearly align with this
13 654 negative correlation. So to test whether Rock Hall can be considered an outlier, linear regression
14 655 was performed on Oudam, Marimba, Sebina, Quela, Duluth and Highfield. This linear regression
15 656 gave a gradient of -2.56 ± 0.45 with an R^2 value of 0.89. The improvement of the fit confirms
16 657 that Rock Hall can be considered an outlier, which is further suggestive of alteration after the
17 658 initial hematite-clay mineral main phase alteration modeled in this paper. In Fig. 10, the position
18 659 of Stoer relative to negative correlation of clay minerals and hematite in Marimba, Sebina,
19 660 Quela, Highfield and Oudam is comparable to the position of the thermochemical models run at
20 661 50 °C relative to those run at higher temperature (75 °C and 100 °C). This shows a possible
21 662 increase in temperature for the formation of the main phase alteration mineral assemblage in
22 663 Stoer.

23 664
24 665 The plotted data in Fig. 10 also show that, although the bulk alteration composition used
25 666 in the thermochemical models varies to a relatively minor extent (Table S4), such small
26 667 variations have a significant influence on the precipitated amounts of clay minerals and hematite
27 668 in the thermochemical model results. However, this variation in modeled mineral abundance
28 669 corresponds to modeled CheMin secondary mineral abundance. In Fig. 10, the shift between the
29 670 trend in the CheMin detections and the trend in the thermochemical models raises the question of
30 671 the role of the CheMin amorphous component, as chemical contributions from the amorphous
31 672 component detected by APXS were included in the chemical alteration compositions used in the
32 673 thermochemical modeling.

33 674
34 675 Here we assume the amorphous component includes sample constituents that cannot be
35 676 identified from CheMin data because crystalline materials in the samples below 1 wt.% are
36 677 included in the amorphous component. The composition of this amorphous composition is
37 678 estimated using CheMin-APXS FULLPAT analysis (Rampe et al., 2020b; Achilles et al., 2020).
38 679 The origin of the X-ray amorphous component is presently not fully understood. However,
39 680 studies have suggested the presence of nanophase Fe-oxides, amorphous sulfates, silicates and
40 681 low amounts of basaltic glass in the amorphous component (Bish et al., 2013; Smith et al., 2019;
41 682 Rapin et al., 2019; Rampe et al., 2020a). A study by Bridges et al (2015b), where Portage soil
42 683 was used in the starting composition, assumed that the amorphous component contained volcanic
43 684 or impact glass, which was then reacted together with olivine to successfully model the alteration
44 685 assemblages observed at Yellowknife Bay. As mentioned in introduction section “Overview of
45 686 the Murray Formation”, the amorphous material is rich in Fe and Si, suggesting the presence of
46 687 nanophase Fe-oxides and amorphous silica (Rampe et al., 2020a; Achilles et al., 2020).
47 688 Considering the models presented in this paper assume that all mineralogy is essentially
48 689 crystalline, the linear shift between modeled and observed trends in Fig. 10 could be attributed to
49 690 an unreacted component of the calculated alteration composition in the drill samples. The
50 691 Marimba, Quela, Sebina, Highfield and Stoer mineral abundances are clustered close to the

thermochemical models run with their alteration compositions. As previously noted, the position of Stoer is comparable to higher temperature (75 °C and 100 °C) thermochemical models.

We tested the idea that the amorphous component might only partially belong to the alteration materials by removing the amorphous component from the CheMin mineral abundances for each drill hole and re-normalizing. This improves the fit between thermochemical model results and CheMin observations with regards to the negative correlation between hematite and clay mineral abundances (Fig. 11). Although there are comparable negative correlations, albeit of different gradients, between the drilled samples analysed by CheMin and the thermochemical models in Fig. 11, the trend with temperature shown in Fig. 10 is lost. This suggests that a part of the amorphous component is reactive. We hypothesize that the CheMin alteration composition was not fully reacted during this phase of alteration. Therefore, this could suggest that the amorphous component had a reactive component and a non-reactive component or that time was insufficient to fully react the amorphous component. The latter could be indicative of the alteration of a volcanic glass (e.g. Wolff-Boenisch et al., 2004). Considering the modeling method assumes complete host rock dissolution and igneous phases are still present in *Curiosity* observations, an unreacted igneous glass component is favored here.

Clay minerals and comparisons to Yellowknife Bay and other Martian terrains, including the Nakhlite Martian Meteorites

The results of this work can be compared to earlier theoretical modeling involving general Martian compositions deduced from Martian meteorite compositions (e.g., Schwenger and Kring, 2009; Filiberto and Schwenger, 2013), the composition of rocks at Yellowknife Bay in Gale crater (Bridges et al., 2015b; Schwenger et al., 2016), and the nakhlite Martian meteorite alteration (Bridges and Schwenger, 2012). Those models are based on varying knowledge of the reaction path, with general assumptions on the alteration paragenesis from orbiters for the first set of models, more precise knowledge of alteration mineral occurrence from CheMin at Yellowknife Bay, and finally a detailed investigation of the alteration assemblage in the nakhlite meteorites. Our study is comparable to the Yellowknife Bay study (Bridges et al., 2015b) in the level of knowledge of the alteration assemblage, and comparisons between the Yellowknife Bay Sheepbed member of the Bradbury Group and the Murray formation are particularly important in understanding the evolution of fluids in the Gale crater sediments. The dioctahedral clay nontronite in our models is a close analog to the dioctahedral smectite identified in Murray (Bristow et al., 2018), therefore, our models have identified a possible diagenetic process to form the hematite-clay mineral assemblage in the Murray formation. The phyllosilicate-bearing assemblage analyzed in the Gale sediments contains no serpentine, chlorite and, at most, traces of illite (Bristow et al., 2018; Rampe et al., 2020b). Phyllosilicates are widespread in the Murray formation and, when present, dominated by smectites.

We start by comparing our assemblage to general Martian alteration deduced from orbiter observations and the MER rovers. The basis for these models were Martian meteorite compositions, e.g., LEW88516 for the models presented by Schwenger and Kring (2009). Based on this poikilitic shergottite composition, the models are dominated by forsteritic olivine (57 vol.%, with contributions from pyroxene (22 vol.%) and plagioclase (16 vol.%) (Gleason et al., 1997). These models showed that there are two important observations: nontronite – which is observed from orbit (Ehlmann et al., 2009; Miliken et al., 2010; Carter et al., 2013) and used as the anchor point for this study – most frequently occurs at intermediate temperatures (~150 °C)

1
2
3 734 and is replaced by chlorite and eventually amphiboles at the higher temperatures of up to 350 °C.
4 735 At lower temperatures (<90 °C) the dominance of forsteritic olivine causes talc formation to
5 736 become more dominant. The system is, however, multi-dimensional, as W/R also influences the
6 737 assemblage, with nontronite generally dominant around W/R of 1,000, being replaced by other
7 738 phyllosilicates and eventually amphiboles towards lower W/R. At the highest W/R (e.g. 10,000)
8 739 hematite dominates, with some nontronite. The results are similar to the results of this study
9 740 focusing on the Murray formation of Gale crater in the comparable pattern of hematite
10 741 dominance at the highest W/R. They differ in the occurrence of talc at the lower temperatures,
11 742 which can be explained by the difference between LEW88516 and our calculated alteration
12 743 compositions for the Murray formation in the MgO concentration (24 wt.% for LEW88516)
13 744 (Schwenzer and Kring, 2009) vs. 5 wt.% (Table S4). This highlights the importance of host rock
14 745 composition for the alteration mineral formation, along with the effect of temperature and
15 746 different W/R ratios. The importance of host rock composition is also highlighted by the fact that
16 747 models with 'Home Plate' MER Spirit rock 'Fastball' composition form nontronite at
17 748 temperatures as low as 13 °C (Filiberto and Schwenzer, 2013). Filiberto and Schwenzer (2013)
18 749 hypothesized that 13 °C was the temperature at 1 km depth if the surface temperature is zero and
19 750 the Martian geothermal gradient is 13 °C (Babeyko and Zharkov, 2000). MgO concentration in
20 751 the assumed host rock is 12 wt.%, significantly lower than for LEW88516, but higher than in this
21 752 study. MgO/Al₂O₃ ratios are 7.6 for LEW88516, 1.5 for Fastball, and 0.97 for the models in this
22 753 study (Table S4). This significantly influences the stability of talc compared to nontronite, but
23 754 also the W/R at which the transition between nontronite and chlorite occurs. Those studies
24 755 (Filiberto and Schwenzer, 2013) were based on well-known host rock compositions, but for the
25 756 Gusev alteration mineral assemblage only orbiter data could be used.

30 757 Previous modeling for the Sheepbed unit (Bridges et al., 2015b) was based on Portage
31 758 Soil with 13 wt% MgO, and an MgO/Al₂O₃ ratio of 0.92 (Blake et al., 2013). Clay minerals
32 759 formed in the first stage of the model, because sulfate minerals were only observed in later veins
33 760 (Bridges et al., 2015b; Schwenzer et al., 2016). The models showed that the secondary mineral
34 761 assemblage formed by the reaction of a CO₂-poor and moderately oxidizing, dilute aqueous
35 762 solution with the sedimentary rocks at 10 – 50 °C and W/R of 100 – 1,000, pH of ~7.5 – 12 (but
36 763 mainly near neutral through most of the reaction range). Modeled phyllosilicates were Fe-
37 764 smectite and chlorite. The bulk phyllosilicate composition was close to saponite stoichiometry,
38 765 which is inferred from CheMin data (Vaniman et al., 2014) though more Fe-rich than the bulk
39 766 clay mineral composition predicted here for the Murray formation at high W/R (Fig. 12).

42 767 The nakhlite meteorite alteration assemblage's reaction pathways were assessed in a
43 768 different way (Bridges and Schwenzer, 2012), because both the host rock and the alteration
44 769 assemblage are known to a high level of detail, including precipitation and re-dissolution
45 770 successions (e.g. Hicks et al., 2014; Bridges et al., 2019). As a consequence of that knowledge,
46 771 the host rock composition could be adapted to match differences in dissolution of individual
47 772 mineral phases. The model concentration has 9 wt.% MgO, and the MgO/Al₂O₃ ratio is 1.9.
48 773 Furthermore, the observations of the alteration mineral succession in the meteorites indicated a
49 774 two-step process, carbonate formation first, followed by the silicate-forming phase. This caused
50 775 a change in the fluid during mineral precipitation, with the silicate-stage fluid being enriched in
51 776 Si, Na, Al, and K. Taking this into account, Fe-smectites form over a wide range of W/R down to
52 777 100 W/R or as low as 10 W/R (Bridges and Schwenzer, 2012). This study on Martian meteorites
53 778 demonstrates the importance in the accuracy of reaction pathway models presented here for

779 observations on the nature of the alteration phase, as well as any indication of differences in
780 alteration conditions for different stages of alteration.

781 For the Sheepbed mudstone of the Bradbury Group there exists the same level of detailed
782 mineralogical knowledge on pre and post alteration mineralogy as we have for the VRR-Murray
783 formation rocks. CheMin X-ray diffraction patterns and SAM evolved gas analyses from
784 mudstone samples demonstrate that phyllosilicate types and abundances vary within the
785 stratigraphic section. Abundant (~20 wt.% of the bulk) Fe³⁺-bearing saponite (a trioctahedral
786 smectite) was identified in mudstone from the Yellowknife Bay formation at the base of the
787 section (Treiman et al., 2014; Vaniman et al., 2014). Mudstone from the Pahrump Hills member,
788 ~60 m up section from Yellowknife Bay and at the base of the Murray formation, has little to no
789 phyllosilicate (up to 8 wt.% of the bulk), and CheMin XRD patterns are consistent with the
790 presence of collapsed smectite (Rampe et al., 2017). Much of the Murray formation
791 stratigraphically above the Pahrump Hills member has abundant (up to 28 wt.% of the bulk)
792 collapsed smectite (Bristow et al., 2018). Both CheMin and SAM data suggest that the structure
793 of the smectite changes from being dominantly trioctahedral (i.e., saponite) lower in the section
794 to being dominantly dioctahedral (i.e., montmorillonite and/or nontronite) higher in the section
795 (Bristow et al., 2018). Duluth was the first sampled analyzed by *Curiosity* to clearly contain only
796 dioctahedral smectite (nontronite, in this case) (Rampe et al., 2020b; McAdam et al., 2020).
797 Phyllosilicates on VRR are distinctly different from those detected in mudstone stratigraphically
798 below the ridge. The abundance of phyllosilicates on VRR is relatively low compared to much of
799 the Murray formation (e.g., Highfield contains 5 wt.% phyllosilicate) (Rampe et al., 2020b).
800 Based on our models, this decrease in phyllosilicates likely relates to the aqueous alteration
801 environment being more oxidizing on the VRR relative to that below (Fig. 10). Furthermore, the
802 phyllosilicates on VRR show a 9.6 Å basal spacing, rather than a 10 Å basal spacing observed in
803 nearly all other phyllosilicate-bearing XRD patterns. This suggests that the phyllosilicate is
804 either a completely collapsed smectite, possibly from alteration in acidic fluids, or that the
805 phyllosilicate is a non-expanding clay mineral, like ferripyrophyllite. SAM data are also
806 consistent with completely collapsed nontronite or ferripyrophyllite on VRR. A similar
807 phyllosilicate was observed in very low abundances in the Oudam sample, drilled
808 stratigraphically above the Pahrump Hills member (Bristow et al., 2018), and the mineralogical
809 similarities between Oudam and Highfield from the gray Jura suggest a comparable aqueous
810 alteration history, as also suggested by our model results (Fig. 10). However, Bristow et al.
811 (2018) hypothesized a detrital origin for ferripyrophyllite at Oudam.

812 There is a notable similarity in trioctahedral saponite observed in Sheepbed mudstone
813 (Vaniman et al., 2014) and the phyllosilicate identified in the nakhlite martian meteorites. Some
814 of these 11 meteorites contain ferric saponite with a trioctahedral structure (Hicks et al., 2014).
815 Trioctahedral saponite as an alteration product of Martian mafic material can be regarded as one
816 of the expected types. Fe/Mg smectites, whether tri or dioctahedral have been identified in
817 numerous places from orbit by reflectance spectroscopy (e.g. Ehlmann et al., 2011; Bibring et al.,
818 2006). In the thermochemical models presented in this paper for the Murray formation, the
819 dioctahedral clay nontronite is dominant at W/R up to 10,000 (Fig. 5 – 7). Similar to the Gale *in*
820 *situ* analyses, serpentine is absent and chlorite is only dominant at extreme W/R, >10,000 in our
821 models. The slightly elevated temperatures of the models in this study (50 – 100 °C) compared to
822 thermochemical modeling for Yellowknife Bay (10 – 50 °C; Bridges et al., 2015b). In addition,
823 thermochemical modeling for Yellowknife Bay suggested a pH range of 7.5 – 12 (Bridges et al.,
824 2015b), which encompasses the pH range of 7.9 – 9.3 for the alteration assemblages modeled in

1
2
3 825 this study. To further compare the results of this study to previous works, we have summed the
4 826 phyllosilicate chemical composition for the models in this paper and included them on a ternary
5 827 plot in Fig. 12, with comparisons to previous modelling at Yellowknife Bay (Bridges et al.,
6 828 2015b) and martian meteorite studies (Hicks et al., 2014). As shown in Fig. 12, the modeled
7 829 phyllosilicates at W/R 10,000 in this study are close to observed Fe-saponites from the nakhlites
8 830 (Lafayette) and Sheepbed unit model saponite (Bridges et al., 2015b). Murray formation
9 831 modeling in this paper at 1,000 and 100 W/R trend towards a nontronite composition, as shown
10 832 in Fig. 12.

13 833 **Comparison to alteration processes in terrestrial environments**

14 834 Impact craters are long recognized as depressions in which lakes can form, and sediments
15 835 accumulate (Cabrol and Grin, 1999; Osinski et al., 2013). Gale crater is no exception, *Curiosity*
16 836 is exploring a rich stratigraphy of lakebed sediments (e.g., Edgar et al., 2020; Fedo et al., 2018;
17 837 Grotzinger et al., 2014, 2015; Hurowitz et al., 2017; introduction section). Our hypothesis is that
18 838 the clay-hematite assemblage is predominantly the result of the first phase of diagenetic
19 839 alteration that affected the sediments brought into Gale crater. The sedimentary textures within
20 840 Gale crater, such as cross-bedding, and coarser units such as conglomerates (Williams et al.,
21 841 2013; introduction section) thereby support the assumption of a dynamic environment with
22 842 freshwater inflow. This underpins our assumption of a dilute, circumneutral 'groundwater-type'
23 843 fluid as the initial pore fluid. The main difference between most of those settings and terrestrial
24 844 analogues is, unfortunately, one of host rock composition as most of Earth's examples are in
25 845 more evolved rocks and/or less iron-rich than the compositionally-basaltic sequences at Gale
26 846 crater.

27 847 Several terrestrial impact craters show sedimentary sequences of lake beds, starting with
28 848 coarse grained sequences gradually transitioning to finer grained sequences, but with
29 849 considerable variation and cyclicity, e.g., the Gardnos impact structure in Norway (Kalleson et
30 850 al., 2008) and the Boltsh impact structure in the Ukraine (Gilmour et al., 2013). The $14.808 \pm$
31 851 0.021 Ma (Schmieder et al., 2018), 24 km diameter Ries impact crater (Nördlingen, Germany)
32 852 has been compared to Gale crater (Arp et al., 2019) as it contains a succession of lake bed
33 853 sediments and was a closed basin. Interestingly, the transport distances for conglomerates at Ries
34 854 are considered to be short due to impact-pre-processing (Arp et al., 2019). The sequence begins
35 855 with clastic sediments with conglomerates and evidence of cyclicity including variation in
36 856 geochemical properties of the lake (oxygen fugacity, salinity, acidity, and new freshwater inflow;
37 857 Jankowski, 1977; Arp et al., 2013), which is similar to observations at Gale of fan deposit
38 858 formation (Williams et al., 2013) and a complex lake chemistry (Hurowitz et al., 2017). This
39 859 shows that sedimentation was accompanied by significant quantities of water and, therefore, a
40 860 groundwater-type scenario as assumed in our study is plausible. Alteration mineralogy of the
41 861 original target rock is consistent with a low-temperature alteration process (Muttik et al., 2008;
42 862 Sapers et al., 2017; Caudill et al., 2021), whereby clays are montmorillonite-type smectites. This
43 863 is comparable to our findings of nontronite, as the difference in clay minerals reflects the
44 864 chemical differences of the host rock: gneiss fragments dominated by feldspars at Ries crater,
45 865 basaltic sediments dominated by mafic phases and plagioclase at Gale crater. The higher Fe-
46 866 content of the rocks at Gale crater, 23 – 30 wt.% (Table S2), compared to the Ries basement
47 867 rocks, 2 – 9 wt.% (von Engelhardt, 1997), explains the different clay mineral chemistry but
48 868 maintains the low-temperature, groundwater-driven clay formation environmental conditions.

1
2
3 869 We next compare to a setting more comparable in chemistry while noting that Fe-
4 870 concentrations at VRR are still higher than those of most terrestrial basalts; Lunar crater
5 871 (Hagerty and Newsom, 2003) and the basalt alteration widely observed in the Deccan trap
6 872 basalts. In the Northeastern part of the Deccan Traps, near Jabalpur, unweathered basalts
7 873 generally contain between 11 and 15 wt.% FeO_{tot} (Peng et al., 1998). Investigation of
8 874 sedimentary and weathered basalt samples by Salil et al. (1997) in the same region near Jabalpur
9 875 show that clay minerals have a similar FeO_{tot} content compared to the basalts: between 10 and 17
10 876 wt.% with a dominance of Fe₂O₃. Iron concentrations between rock and alteration assemblage
11 877 appear constant, if not slightly higher in the sediments and basaltic alteration assemblages, which
12 878 is comparable to our observations where Fe in the fluid is generally very low (~10⁻⁹) at 10,000
13 879 W/R (Fig. S1). For the Deccan Traps, Fe-concentrations in runoff water of the region appear
14 880 comparably very low as they are not reported for the region (Gupta et al., 2011), or more widely
15 881 in cold and warm spring waters as well as runoff across the Deccan (Minissale et al., 2000).
16 882 Clay-mineralogy in the sediments and Deccan alteration is Fe, Mg-rich smectites, which the
17 883 authors describe as similar to but not quite nontronitic as the Fe-content is below 50% (Salil et
18 884 al., 1997). This shows that water-dominated, groundwater-rock reactions such as proposed here
19 885 occur in weathering or diagenetic environments and are similar to the observed clay mineralogy
20 886 at the Gale site and in our models.

24 25 887 CONCLUSIONS

26 888 In this paper we showed that local element mobility rather than large scale, basin-wide
27 889 fluid movement is the most likely alteration mechanism for the main phase of alteration in the
28 890 Murray formation. For this, we derived chemical alteration compositions using data from
29 891 CheMin (Achilles et al., 2020; Rampe et al., 2020b) and APXS (Thompson et al., 2020) and
30 892 found them to be very similar for the Murray formation below as well as on Vera Rubin ridge.
31 893 After this main phase, based on the age dating and the local nature of its occurrence, a younger
32 894 alteration event caused the observed akaganeite and jarosite, whereby we assume that Fe was
33 895 remobilized from the mineral assemblages in our models (i.e. Fe-sulfides).

36 896 Our thermochemical modeling results indicate that the alteration that produced the early
37 897 diagenetic hematite-clay mineral assemblage in the Murray formation, below and on VRR, can
38 898 be explained by reaction of dilute brine with the calculated alteration compositions at
39 899 temperatures between 50 and an upper limit of 100 °C, and at a notably high W/R of
40 900 approximately 10,000 with pH ranging from 7.9 to 9.3. Modeling at 25 °C produces goethite,
41 901 which could transition to hematite at a later stage however, this phase together with the relative
42 902 abundances with the clay content are not directly comparable to *Curiosity* observations. We
43 903 interpret the high W/R as enhanced groundwater flow through this part of the Gale sedimentary
44 904 sequence compared to that in the Bradbury Group and its Yellowknife Bay mudstone, where
45 905 lower temperature alteration (20 – 50 °C) with a broader pH range of 7.5 – 12 (Bridges et al.,
46 906 2015b). This further constraint on the fluid temperature and pH in the models presented in this
47 907 paper is likely to have important implications for microbial habitability.

51 908 The trends between the modeled and observed phyllosilicate and hematite abundances are
52 909 comparable, but not exact due to our model not precipitating metastable phases such as the
53 910 CheMin amorphous component. We interpret the amorphous component to have partially
54 911 contributed to the phase of alteration modeled in this study. Future work is necessary to
55 912 determine the composition and origin of the CheMin amorphous component, and thus how its

1
2
3 913 chemistry can be most appropriately used in thermochemical modeling studies. We will continue
4 914 modeling the Gale crater sedimentary mineral assemblage which in future work we aim to extend
5 915 from the Bradbury and Murray-VRR, into the clay-bearing Glen Torridon and overlying Sulfate
6 916 Units.
7
8
9
10
11
12
13
14
15
16
17
18
19
20
21
22
23
24
25
26
27
28
29
30
31
32
33
34
35
36
37
38
39
40
41
42
43
44
45
46
47
48
49
50
51
52
53
54
55
56
57
58
59
60

For Peer Review Only

1
2
3 917 **ACKNOWLEDGMENTS, SAMPLES, AND DATA**
4

5 918 SMRT, SPS and JCB were funded by UK Space Agency grant ST/S001522/1. CCB was funded
6 919 through the STFC doctoral training grant to the OU. ACM acknowledges funding support from
7 920 the NASA ROSES MSL Participating Scientist Program. Unless stated otherwise, mineralogical
8 921 and chemical data used in the modeling from the Mars Science Laboratory *Curiosity* rover are
9 922 from the NASA PDS. Data necessary to reproduce the thermochemical modeling results shown
10 923 in this paper is available on The Open University data repository
11 924 (<https://doi.org/10.21954/ou.rd.14892132>). Authors would like to thank Jim Palandri for CHIM-
12 925 XPT access and support. Support from the scientists, engineers, colleagues in operations roles,
13 926 and staff of NASA Mars Science Laboratory Mission is gratefully acknowledged. SMRT would
14 927 like to thank Nisha Ramkissoon for thermochemical modeling discussions. This manuscript
15 928 benefitted from reviews by Patrick Gasda, Allan Treiman, and Gordon Osinski. Previous
16 929 versions of this manuscript benefitted from reviews by Benjamin Tutolo, Jake Crandall, and
17 930 three anonymous reviewers.
18
19
20 931
21
22
23
24
25
26
27
28
29
30
31
32
33
34
35
36
37
38
39
40
41
42
43
44
45
46
47
48
49
50
51
52
53
54
55
56
57
58
59
60

1
2
3 **932 References**
4

- 5 933 Achilles C.N., Rampe E.B., Downs R.T., Bristow T.F., Ming D.W., Morris R.V., Vaniman D.T.,
6 934 Blake D.F., Yen A.S., McAdam A.C., Sutter B., Fedo C.M., Gwizd S., Thompson L.M.,
7 935 Gellert R., Morrison S.M., Treiman A.H., Crisp J.A., Gabriel T.S.J., Chipera S.J., Hazen
8 936 R.M., Craig P.I., Thorpe M.T., Des Marais D.J., Grotzinger J.P., Tu V.M., Castle N.,
9 937 Downs G.W., Peretyazhko T.S., Walroth R.C., Sarrazin P., and Morookian J.M. 2020.
10 938 Mineralogy of ancient fluvial-lacustrine sediments in Gale crater, Mars: Evidence for
11 939 multiple diagenetic episodes. *Journal of Geophysical Research: Planets*, 125,
12 940 e2019JE006295.
- 14 941 Anderson R.B., and Bell III, J.F. 2010. Geologic mapping and characterization of Gale Crater
15 942 and implications for its potential as a Mars Science Laboratory landing site. *Mars* 5, 76-
16 943 128.
- 18 944 Arp G., Schultz S., Karius V., and Head III J.W. 2019. Ries impact crater sedimentary
19 945 conglomerates: Sedimentary particle 'impact pre-processing', transport distances and
20 946 provenance, and implications for Gale crater conglomerates, Mars. *Icarus*, 321, pp.531-
21 947 549.
- 23 948 Babeyko A.Y., and Zharkov V.N. 2000. Martian crust: a modeling approach. *Physics of the*
24 949 *Earth and planetary interiors*, 117(1-4), 421-435.
- 26 950 Baron F., Gaudin A., Lorand J.P., and Mangold N. 2019. New Constraints on Early Mars
27 951 Weathering Conditions from an Experimental Approach on Crust Simulants. *Journal of*
28 952 *Geophysical Research: Planets*, 124, 1783-1801.
- 30 953 Bedford C.C., Bridges J.C., Schwenzer S.P., Wiens R.C., Rampe E.B., Frydenvang J., and Gasda
31 954 P.J. 2019. Alteration trends and geochemical source region characteristics preserved in
32 955 the fluvio-lacustrine sedimentary record of Gale crater, Mars. *Geochimica et*
33 956 *Cosmochimica Acta*, 246, 234-266. doi:10.1016/j.gca.2018.11.031.
- 35 957 Bennett K.A., Edgett K., Fey D., Edgar L.A., Fraeman A., McBride M., and Edwards C. 2018.
36 958 Fine-Scale Textural Observations at Vera Rubin Ridge, Gale Crater, from the Mars Hand
37 959 Lens Imager (MAHLI). In *Proceedings 49th Lunar and Planetary Science Conference*,
38 960 *The Woodlands, TX (Vol. 49, p. 1769)*.
- 40 961 Blake D.F., Morris R.V., Kocurek G., Morrison S.M., Downs R.T., Bish D., Ming D.W., Edgett
41 962 K.S., Rubin D., Goetz W., Madsen M.B., Sullivan R., Gellert R., Campbell I., Treiman
42 963 A.H., McLennan S.M., Yen A.S., Grotzinger J., Vaniman D.T., Chipera S.J., Achilles
43 964 C.N., Rampe E.B., Sumner D., Meslin P.-Y., Maurice S., Forni O., Gasnault O., Fisk M.,
44 965 Schmidt M., Mahaffy P., Leshin L.A., Glavin D., Steele A., Freissinet C., Navarro-
45 966 González R., Yingst R.A., Kah L.C., Bridges N., Lewis K.W., Bristow T.F., Farmer J.D.,
46 967 Crisp J.A., Stolper E.M., Des Marais D.J., Sarrazin P., and MSL Science Team 2013.
47 968 Curiosity at Gale crater, Mars: Characterization and analysis of the Rocknest sand
48 969 shadow. *Science*, 341(6153), p.1239505.
- 51 970 Blake D., Vaniman D., Achilles C., Anderson R., Bish D., Bristow T., Chen C., Chipera S., Crisp
52 971 J., Des Marais D., Downs R.T., Farmer J., Feldman S., Fonda M., Gailhanou M., Ma H.,
53 972 Ming D.W., Morris R.V., Sarrazin P., Stolper E., Treiman A., and Yen A. 2012.
54 973 Characterization and calibration of the CheMin mineralogical instrument on Mars
55 974 Science Laboratory. *Space Sci. Rev.* 170(1-4), 341-399.

- 1
2
3 975 Bibi I., Singh B., and Silvester E. 2011. Akaganéite (β -FeOOH) precipitation in inland acid
4 976 sulfate soils of south-western New South Wales (NSW), Australia. *Geochimica et*
5 977 *Cosmochimica Acta*, 75(21), 6429-6438.
- 7 978 Bibring J.P., Langevin Y., Mustard J.F., Poulet F., Arvidson R., Gendrin A., Gondet B., Mangold
8 979 N., Pinet P., Forget F., and the OMEGA team 2006. Global mineralogical and aqueous
9 980 Mars history derived from OMEGA/Mars Express data. *Science*, 312(5772), 400-404.
- 11 981 Bish D.L., Blake D.F., Vaniman D.T., Chipera S.J., Morris R.V., Ming D.W., Treiman A.H.,
12 982 Sarrazin P., Morrison S.M., Downs R.T., Achilles C.N., Yen A.S., Bristow T.F., Crisp
13 983 J.A., Morookian J.M., Farmer J.D., Rampe E.B., Stolper E.M., Spanovich N., and MSL
14 984 Science Team 2013. X-ray diffraction results from Mars Science Laboratory: Mineralogy
15 985 of Rocknest at Gale crater. *Science*, 341(6153), p.1238932.
- 17 986 Bridges J.C., and Schwenzer S.P. 2012. The nakhlite hydrothermal brine on Mars. *Earth and*
18 987 *Planetary Science Letters*, 359, 117-123.
- 20 988 Bridges J.C., Schwenzer S.P., Leveille R., Wiens R.C., McAdam A., Conrad P., and Kelley S.P.
21 989 2015a. Hematite Formation in Gale Crater. In *Lunar and Planetary Science Conference*,
22 990 *The Woodlands, TX (Vol. 46, p. 1769)*.
- 24 991 Bridges J.C., Schwenzer S.P., Leveille R., Westall F., Wiens R.C., Mangold N., Bristow T.,
25 992 Edwards P., and Berger G. 2015b. Diagenesis and Clay mineral Formation in Gale
26 993 Crater, Mars. *J. Geophys. Res. Planets*, 120, 1-19, doi:10.1002/2014JE004757.
- 28 994 Bridges J.C., Hicks, L.J., and Treiman A.H. 2019. Carbonates on Mars. In *Volatiles in the*
29 995 *Martian Crust*. 1st edition. Elsevier. Editors Filiberto and Schwenzer, pp 426.
- 31 996 Bristow T.F., Rampe E.B., Achilles C.N., Blake D.F., Chipera S.J., Craig P., Crisp J.A., Des
32 997 Marais D.J., Downs R.T., Gellert R., Grotzinger J.P., Gupta S., Hazen R.M., Horgan B.,
33 998 Hogancamp J.V., Mangold N., Mahaffy P.R., McAdam A.C., Ming D.W., Morookian
34 999 J.M., Morris R.V., Morrison S.M., Treiman A.H., Vaniman D.T., Vasavada A.R., and
35 1000 Yen, A.S. 2018. Clay mineral diversity and abundance in sedimentary rocks of Gale
36 1001 crater, Mars. *Science Advances* (6), eaar3330.
- 38 1002 Cabrol N.A., and Grin E.A. 1999. Distribution, classification, and ages of Martian impact crater
39 1003 lakes. *Icarus*, 142(1), pp.160-172.
- 41 1004 Carter J., Poulet F., Bibring J.P., Mangold N., and Murchie S. 2013. Hydrous minerals on Mars
42 1005 as seen by the CRISM and OMEGA imaging spectrometers: Updated global view.
43 1006 *Journal of Geophysical Research: Planets*, 118(4), 831-858.
- 45 1007 Catalano J.G. 2013. Thermodynamic and mass balance constraints on iron-bearing phyllosilicate
46 1008 formation and alteration pathways on early Mars. *Journal of Geophysical Research:*
47 1009 *Planets*, 118(10), 2124-2136.
- 49 1010 Catling D.C., and Moore J.M. 2003. The nature of coarse-grained crystalline hematite and its
50 1011 implications for the early environment of Mars. *Icarus*, 165(2), 277-300,
51 1012 [http://dx.doi.org/10.1016/S0019-1035\(03\)00173-8](http://dx.doi.org/10.1016/S0019-1035(03)00173-8).
- 53 1013 Caudill C., Osinski G. R., Greenberger R. N., Tornabene L. L., Longstaffe F. J., Flemming R L.,
54 1014 B. L. and Ehlmann B. 2021. Origin of the degassing pipes at the Ries impact structure

- 1
2
3 1015 and implications for impact-induced alteration on Mars and other planetary bodies.
4 1016 Meteoritics & Planetary Science 56:404–422.
- 6 1017 Chevrier V., Poulet F., and Bibring J.-P. 2007. Early geochemical environment of Mars as
7 1018 determined from thermodynamics of phyllosilicates. *Nature*, **448**: 60–63.
- 9 1019 Cornell and Schwertmann 2006. *The Iron Oxides: Structure, Properties, Reactions, Occurrences*
10 1020 *and Uses*, John Wiley & Sons.
- 11 1021 Deer W.A., Howie R.A., and Zussman J. 1992. *An introduction to the rock-forming minerals.*
12 1022 2nd edition. The Mineralogical Society, London.
- 14 1023 Deer W.A., Howie R.A., and Zussman J. 2013. *An introduction to the rock-forming minerals.*
15 1024 3rd edition. The Mineralogical Society, London.
- 17 1025 Edgar L.A., Fraeman A., Gupta S., Fedo C., Grotzinger J.P., Stack K., Bennett K.A., Sun V.Z.,
18 1026 Banham S., Stein N., Edgett K.S., Rubin D.M., House C.H., and Van Beek J. 2018. A
19 1027 Lacustrine Environment Recorded at Vera Rubin Ridge: Overview of the Sedimentology
20 1028 and Stratigraphy observed by the Mars Science Laboratory Curiosity Rover. In
21 1029 *Proceedings AGU*, Washington, D.C.
- 23 1030 Edgar L.A., Fedo C.M., Gupta S., Banham S.G., Fraeman A.A., Grotzinger J.P., Stack K.M.,
24 1031 Stein N.T., Bennett K.A., Rivera-Hernández F., Sun V.Z., Edgett K.S., Rubin D.M.,
25 1032 House C., and van Beek J. 2020. A lacustrine paleoenvironment recorded at Vera Rubin
26 1033 ridge, Gale crater: Overview of the sedimentology and stratigraphy observed by the Mars
27 1034 Science Laboratory Curiosity rover. *Journal of Geophysical Research: Planets*, 125,
28 1035 e2019JE006307.
- 31 1036 Ehlmann B.L., Mustard J.F., Swayze G.A., Clark R.N., Bishop J.L., Poulet F., Des Marais D.J.,
32 1037 Roach L.H., Milliken R.E., Wray J.J., Barnouin-Jha O., and Murchie S.L. 2009.
33 1038 Identification of hydrated silicate minerals on Mars using MRO-CRISM: Geologic
34 1039 context near Nili Fossae and implications for aqueous alteration. *Journal of Geophysical*
35 1040 *Research: Planets*, 114(E2).
- 37 1041 Ehlmann B.L., Mustard J.F., Murchie S.L., Bibring J.P., Meunier A., Fraeman A.A., and
38 1042 Langevin Y. 2011. Subsurface water and clay mineral formation during the early history
39 1043 of Mars. *Nature*, 479(7371), 53.
- 41 1044 Filiberto J., and Schwenzer S.P. 2013. Alteration mineralogy of Home Plate and Columbia
42 1045 Hills—Formation conditions in context to impact, volcanism, and fluvial activity.
43 1046 *Meteoritics & Planetary Science*, 48(10), 1937-1957.
- 45 1047 Fraeman A.A., Arvidson R.E., Catalano J.G., Grotzinger J.P., Morris R.V., Murchie S.L., Stack
46 1048 K.M., Humm D.C., McGovern J.A., Seelos F.P., Seelos K.D., and Viviano C.E. 2013. A
47 1049 hematite-bearing layer in Gale Crater, Mars: Mapping and implications for past aqueous
48 1050 conditions. *Geology*, 41(10), 1103-1106.
- 50 1051 Fraeman A.A., Ehlmann B.L., Arvidson R.E., Edwards C.S., Grotzinger J.P., Milliken R.E.,
51 1052 Quinn D.P., and Rice M.S. 2016. The Stratigraphy and Evolution of Lower Mt. Sharp
52 1053 from Spectra, Morphological, and Thermophysical Orbital Datasets. *Journal of*
53 1054 *Geophysical Research: Planets*, 121(9), 1713-1736.

- 1
2
3 1055 Fraeman A.A., Edgar L.A., Rampe E.B., Thompson L.C., Frydenvang J., Fedo C., Catalano J.G.,
4 1056 Dietrich W.E., Gabriele, T.S.J., Vasavada A.R., Grotzinger J.P., L'Haridon J., Mangold N.,
5 1057 Sun V.Z., House C.H., Bryk A.B., Hardgrove C., Czarnecki S., Stack K.M., Morris R.V.,
6 1058 Arvidson R.E., Banham S.G., Bennett K.A., Bridges J.C., Edwards C.S., Fischer W.W.,
7 1059 Fox V.K., Gupta S., Horgan B.H.N., Jacob S.R., Johnson J.R., Johnson S.S., Rubin D.M.,
8 1060 Salvatore M.R., Schwenzer S.P., Siebach K.L., Stein N.T., Turner S.M.R., Wellington
9 1061 D.F., Wiens R.C., Williams A.J., David G., and Wong G.M. 2020. Evidence for a
10 1062 Diagenetic Origin of Vera Rubin Ridge, Gale Crater, Mars: Summary and Synthesis of
11 1063 *Curiosity's* Exploration Campaign. *Journal of Geophysical Research: Planets*, 125,
12 1064 e2020JE006527.
- 15 1065 Frydenvang J., Gasda P.J., Hurowitz J.A., Grotzinger J.P., Wiens R.C., Newsom H.E., Edgett
16 1066 K.S., Watkins J., Bridges J.C., Maurice S., Fisk M.R., Johnson J.R., Rapin W., Stein
17 1067 N.T., Clegg S.M., Schwenzer S.P., Bedford C.C., Edwards P., Mangold N., Cousin A.,
18 1068 Anderson R.B., Payré V., Vaniman D., Blake D.F., Lanza N.L., Gupta S., Van Beek J.,
19 1069 Sautter V., Meslin P.-Y., Rice M., Milliken R., Gellert R., Thompson L., Clark B.C.,
20 1070 Sumner D.Y., Fraeman A.A., Kinch K.M., Madsen M.B., Mitrofanov I.G., Jun I., Calef
21 1071 F., and Vasavada A.R. 2017. Diagenetic silica enrichment and late-stage groundwater
22 1072 activity in Gale crater, Mars. *Geophysical Research Letters*, 44(10), 4716-4724.
- 25 1073 Frydenvang J., Mangold N., Wiens R.C., Fraeman A.A., Edgar L.A., Fedo C., L'Haridon J.,
26 1074 Bedford C.C., Gupta S., Grotzinger J.P., Bridges J.C., Clark B.C., Rampe E.B., Gasnault
27 1075 O., Maurice S., Gasda P.J., Lanza N.L., Olilla A.M., Meslin P.-Y., Payré V., Calef F.,
28 1076 Salvatore M., and House C.M. 2020. The Chemostratigraphy of the Murray Formation
29 1077 and Role Of Diagenesis at Vera Rubin Ridge in Gale Crater, Mars, as Observed by the
30 1078 ChemCam Instrument. *Journal of Geophysical Research: Planets*, 125, e2019JE006320.
- 32 1079 Ganguly J. 2008. *Thermodynamics in Earth and Planetary Science*. Springer. Berlin-Heidelberg.
33 1080 501 p.
- 35 1081 Gilmour I., Jolley D.W., Watson J. S., Gilmour M. A., and Kelley S. P. 2013. Post-impact
36 1082 heating of a crater lake. In: *European Planetary Science Congress 2013*, 08-13 Sep 2013,
37 1083 London.
- 39 1084 Gleason J.D., Kring D.A., Hill D.H., and Boynton W.V. 1997. Petrography and bulk chemistry
40 1085 of Martian lherzolite LEW88516. *Geochimica et Cosmochimica Acta*, 61(18), 4007-
41 1086 4014.
- 43 1087 Griffith L.L., and Shock E.L. 1995. A geochemical model for the formation of hydrothermal
44 1088 carbonates on Mars. *Nature*, **377**: 406–408.
- 46 1089 Griffith L.L., and Shock E.L., 1997. Hydrothermal hydration of Martian crust: Illustration via
47 1090 geochemical model calculations. *Journal of Geophysical Research*, **102**: 9135–9143.
- 48 1091 Grotzinger J.P., Sumner D.Y., Kah L.C., Stack K., Gupta S., Edgar L., Rubin D., Lewis K.,
49 1092 Schieber J., Mangold N., Milliken R., Conrad P.G., DesMarais D., Farmer J., Siebach K.,
50 1093 Calef III F., Hurowitz J., McLennan S.M., Ming D., Vaniman D., Crisp J., Vasavada A.,
51 1094 Edgett K.S., Malin M., Blake D., Gellert R., Mahaffy P., Wiens R.C., Maurice S., Grant
52 1095 J.A., Wilson S., Anderson R.C., Beegle L., Arvidson R., Hallet B., Sletten R.S., Rice M.,
53 1096 Bell III J., Griffes J., Ehlmann B., Anderson R.B., Bristow T.F., Dietrich W.E., Dromart
54 1097 G., Eigenbrode J., Fraeman A., Hardgrove C., Herkenhoff K., Jandura L., Kocurek G.,

- 1
2
3 1098 Lee S., Leshin L.A., Leveille R., Limonadi D., Maki J., McCloskey S., Meyer M., Minitti
4 1099 M., Newsom H., Oehler D., Okon A., Palucis M., Parker T., Rowland S., Schmidt M.,
5 1100 Squyres S., Steele A., Stopler E., Summons R., Treiman A., Williams R., Yingst A., and
6 1101 MSL Science Team 2014. A Habitable Fluvio-Lacustrine Environment at Yellowknife
7 1102 Bay, Gale Crater, Mars. *Science*, 343(6169), p.1242777.
- 8
9 1103 Grotzinger J.P., Gupta S., Malin M.C., Rubin D.M., Schieber J., Siebach K., Sumner D.Y., Stack
10 1104 K.M., Vasavada A.R., Arvidson R.E., Calef III F., Edgar L., Fischer W.F., Grant J.A.,
11 1105 Griffes J., Kah L.C., Lamb M.P., Lewis K.W., Mangold N., Minitti M.E., Palucis M.,
12 1106 Rice M., Williams R.M.E., Yingst R.A., Blake D., Blaney D., Conrad P., Crisp J.,
13 1107 Dietrich W.E., Dromart G., Edgett K.S., Ewing R.C., Gellert R., Hurowitz J.A., Kocurek
14 1108 G., Mahaffy P., McBride M.J., McLennan S.M., Mischna M., Ming D., Milliken R.,
15 1109 Newsom H., Oehler D., Parker T.J., Vaniman D., Wiens R.C., and Wilson S.A. 2015.
16 1110 Deposition, exhumation, and paleoclimate of an ancient lake deposit, Gale crater, Mars.
17 1111 *Science*, v. 350, no. 6257, p. aac7575.
- 18
19 1112 Gupta H., Chakrapani G.J., Selvaraj K., and Kao S.J. 2011. The fluvial geochemistry,
20 1113 contributions of silicate, carbonate and saline-alkaline components to chemical
21 1114 weathering flux and controlling parameters: Narmada River (Deccan Traps), India.
22 1115 *Geochimica et Cosmochimica Acta*, 75(3), pp.800-824.
- 23
24 1116 Gwizd S., Fedo C., Grotzinger J., Edgett K., Rivera-Hernandez F., and Stein N. 2018.
25 1117 Depositional History of the Hartmann's Valley Member, Murray Formation, Gale Crater,
26 1118 Mars. In *Lunar and Planetary Science Conference, The Woodlands, TX (Vol. 49, p.*
27 1119 *2150)*.
- 28
29 1120 Hagerty J.J., and Newsom H.E. 2003. Hydrothermal alteration at the Lonar Lake impact
30 1121 structure, India: Implications for impact cratering on Mars. *Meteoritics & Planetary*
31 1122 *Science*, 38(3), pp.365-381.
- 32
33 1123 Harker R.I. 1959. The synthesis and stability of tilleyite, $\text{Ca}_5\text{Si}_2\text{O}_7(\text{CO}_3)_2$. *American Journal of*
34 1124 *Science*, 257(9), 656-667.
- 35
36 1125 Hausrath E.M., Ming D.W., Peretyazhko T. S., and Rampe E. B. 2018. Reactive transport and
37 1126 mass balance modeling of the Stimson sedimentary formation and altered fracture zones
38 1127 constrain diagenetic conditions at Gale crater, Mars.– *Earth and Planetary Science Letter*,
39 1128 491, 1–10.
- 40
41 1129 Heydari E., Parker T.J., Calef III F.J., Schroeder J.F., Van Beek J., Rowland S.K., and Fairen
42 1130 A.G. 2018. Characteristics and the Origin of the Vera Rubin Ridge, Gale Crater, Mars. In
43 1131 *Proceedings Lunar and Planetary Science Conference, The Woodlands, TX (Vol. 49, p.*
44 1132 *1817)*.
- 45
46 1133 Hicks L.J., Bridges J.C., and Gurman S.J. 2014. Ferric saponite and serpentine in the nakhlite
47 1134 martian meteorites. *Geochimica et Cosmochimica Acta*, 136, 194-210.
- 48
49 1135 Holland T.J.B., and Powell R. 1998. An internally consistent thermodynamic data set for phases
50 1136 of petrological interest. *J. Metamorph. Geol.* 16, 309–343.
- 51
52 1137 Horgan B.H.N., Johnson J.R., Fraeman A.A., Rice M.S., Seeger C., Bell III J.F., Bennett K.A.,
53 1138 Cloutis E.A., Edgar L.A., Frydenvang J., Grotzinger J.P., L'Haridon J., Jacob S.R.,
54 1139 Mangold N., Rampe E.B., Rivera-Hernandez F., Sun V.Z., Thompson L.M., and

- 1
2
3 1140 Wellington D. 2020. Diagenesis of Vera Rubin Ridge, Gale Crater, Mars from Mastcam
4 1141 Multispectral Images. *Journal of Geophysical Research: Planets*, 125, e2019JE006322.
- 6 1142 Hurowitz J.A., Grotzinger J.P., Fischer W.W., McLennan S.M., Milliken R.E., Stein N.,
7 1143 Vasavada A.R., Blake D.F., Dehouck E., Eigenbrode J.L., Fairén A.G., Frydenvang J.,
8 1144 Gellert R., Grant J.A., Gupta S., Herkenhoff K.E., Ming D.W., Rampe E.B., Schmidt
9 1145 M.E., Siebach K.L., Stack-Morgan K., Sumner D.Y., and Wiens R.C. 2017. Redox
10 1146 stratification of an ancient lake in Gale Crater, Mars. *Science*, v. 356, no. 6341, p.
11 1147 eeah6849.
- 13 1148 Jankowski B. 1977. Die Postimpakt-Sedimente in der Forschungsbohrung Nördlingen 1973. -
14 1149 *Geologica Bavarica*, 75: 21-36.
- 16 1150 Kalleson E., Dypvik H., and Naterstad J. 2008. Postimpact sediments in the Gardnos impact
17 1151 structure, Norway. *SPECIAL PAPERS-GEOLOGICAL SOCIETY OF AMERICA*, 437,
18 1152 p.19.
- 20 1153 Kühn M. 2004. Reactive flow modeling of hydrothermal systems. *Lect. Notes Earth Sci.* 103,
21 1154 261 p.
- 23 1155 L'Haridon J., Mangold N., Meslin P.Y., Johnson J.R., Rapin W., Forni O., Cousin A., Payré V.,
24 1156 Dehouck E., Nachon M., Le Deit L., Gasnault O., Maurice S., and Wiens R.C. 2018.
25 1157 Chemical variability in mineralized veins observed by ChemCam on the lower slopes of
26 1158 Mount Sharp in Gale crater, Mars. *Icarus*, 311, 69-86.
- 28 1159 L'Haridon J., Mangold N., Fraeman A.A., Johnson J.R., Cousin A., Rapin W., David G.,
29 1160 Dehouck E., Sun V., Frydenvang J., Gasnault O., Gasda P., Lanza N., Forni O., Meslin
30 1161 P.-Y., Schwenzer S.P., Bridges J., Horgan B., House C.H., Salvatore M., Maurice S., and
31 1162 Wiens R.C. 2020. Iron Mobility During Diagenesis the Vera Rubin Ridge, Gale Crater,
32 1163 Mars. *Journal of Geophysical research: Planets*, 125, e2019JE006299.
- 34 1164 Mangold N., Dehouck E., Fedo C., Forni O., Achilles C., Bristow T., Downs R.T., Frydenvang
35 1165 J., Gasnault O., L'Haridon J., Le Deit L., Maurice S., McLennan S.M., Meslin P.-Y.,
36 1166 Morrison S., Newsom H.E., Rampe E., Rapin W., Rivera-Hernandez F., Salvatore M.,
37 1167 and Wiens R.C. 2019a. Chemical alteration of fine-grained sedimentary rocks at Gale
38 1168 crater. *Icarus*, 321, 619-631.
- 40 1169 Mangold N., Cousin A., Dehouck E., Forni O., Fraeman A., Frydenvang J., Gasnault O., Johnson
41 1170 J., Le Deit J.L., L'Haridon J., Le Mouélic S., Maurice S., McLennan S.M., Meslin P.-Y.,
42 1171 Hewsom H.E., Rapin W., Rivera-Hernandez F., and Wiens R.C. 2019b.
43 1172 Chemostratigraphy of Fluvial and Lacustrine Sedimentary Rocks at Gale Crater Using
44 1173 Chemcam Onboard the Curiosity Rover. *Ninth International Conference on Mars*.
45 1174 Abstract #6078.
- 48 1175 Marion D. M., Catling D. C., and Karegel J. S. 2003. Modeling aqueous ferrous iron chemistry at
49 1176 low temperatures with application to Mars. *Geochim. Cosmochim. Acta*, 22, 4251-4266.
- 51 1177 Martin P.E., Farley K.A., Baker M.B., Malespin C.A., Schwenzer S.P., Cohen B.A., Mahaffy
52 1178 P.R., McAdam A.C., Ming D.W., Vasconcelos P.M., and Navarro-González R. 2017. A
53 1179 two-step K-Ar experiment on Mars: Dating the diagenetic formation of jarosite from
54 1180 Amazonian groundwaters. *Journal of Geophysical Research: Planets*, 122(12), 2803-
55 1181 2818.

- 1
2
3 1182 McAdam A.C., Sutter B., Douglas Archer P., Franz H.B., Wong G.M., Lewis J.M.T.,
4 1183 Eigenbrode J.L., Stern J.C., Knudson C.A., Clark J.V., Andrejkovičová S., Ming D.W.,
5 1184 Morris R.V., Achilles C.N., Rampe E.B., Bristow T.F., Navarro-González R., Mahaffy
6 1185 P.R., Thompson L.M., Gellert R., Williams A.J., House C.H., and Johnson S.S. 2020.
7 1186 Constraints on the Mineralogy and Geochemistry of the Vera Rubin Ridge, Gale Crater,
8 1187 Mars From Mars Science Laboratory Sample Analysis at Mars Evolved Gas Analysis.
9 1188 Journal of Geophysical Research: Planets, 125, 2019JE006309.
- 11 1189 McAdam A. C., Zolotov M. Y., Mironenko M. V. and Sharp G. 2008. Formation of silica by low
12 1190 temperature acid alteration of Martian rocks: Physical-chemical constraints. Journal of
13 1191 Geophysical Research, **113**: doi10.1029/2007JE003056.
- 15 1192 Melwani Daswani M., Schwenzer S.P., Reed M.H., Wright I.P., and Grady M.M. 2016.
16 1193 Alteration minerals, fluids, and gases on early Mars: Predictions from 1-D flow
17 1194 geochemical modeling of mineral assemblages in meteorite ALH 84001. Meteoritics &
18 1195 Planetary Science, 51(11), 2154-2174.
- 21 1196 Meslin P.Y., Gasda P., L'Haridon J., Forni O., Lanza N., Lamm S., Johnson J.R., Wiens R.C.,
22 1197 Thompson L., Rapin W., Gasnault O., Cousin A., Mangold N., Dehouck E., Maurice S.,
23 1198 Lasue J., and Frydenvang J. 2018. Detection of Hydrous Manganese and Iron Oxides
24 1199 with Variable Phosphorus and Magnesium Contents in the Lacustrine Sediments of the
25 1200 Murray Formation, Gale, Mars. In Lunar and Planetary Science Conference (Vol. 49, p.
26 1201 1447).
- 28 1202 Milliken R.E., Grotzinger J.P., and Thomson B.J. 2010. Paleoclimate of Mars as captured by the
29 1203 stratigraphic record in Gale Crater. Geophysical Research Letters, v. 37, no. 4, p.
30 1204 L04201.
- 32 1205 Minissale A., Vaselli O., Chandrasekharam D., Magro G., Tassi F., and Casiglia A. 2000. Origin
33 1206 and evolution of “intracratonic” thermal fluids from central-western peninsular India,
34 1207 Earth Planet. Sci. Lett., 181(3), 377–394.
- 36 1208 Misra K.C. 2012. Introduction to geochemistry: principles and applications. John Wiley & Sons.
- 38 1209 Morrison S.M., Downs R.T., Blake D.F., Vaniman D.T., Ming D.W., Hazen R.M., Treiman
39 1210 A.H., Achilles C.N., Yen A.S., Morris R.V., Rampe E.B., Bristow T.F., Chipera S.J.,
40 1211 Sarrazin P.C., Gellert R., Fendrich K.V., Morookian J.M., Farmer J.D., Des Marais D.J.,
41 1212 and Craig P.I. 2018. Crystal chemistry of martian minerals from Bradbury Landing
42 1213 through Naukluft Plateau, Gale crater, Mars. Am. Mineral. 103(6), 857-871.
- 44 1214 Murchie S., Arvidson R., Bedini P., Beisser K., Bibring J.P., Bishop J., Boldt J., Cavender P.,
45 1215 Choo T., Clancy R.T., Darlington E.H., Des Marais D., Espiritu R., Fort D., Green R.,
46 1216 Guinness E., Hayes J., Hash C., Heffernan K., Hemmler J., Heyler G., Humm D.,
47 1217 Hutcheson J., Izenberg N., Lee R., Lees J., Lohr D., Malaret E., Martin T., McGovern
48 1218 J.A., McGuire P., Morris R., Mustard J., Pelkey S., Rhodes E., Robinson M., Roush T.,
49 1219 Schaefer E., Seagrave G., Seelos F., Silverglate P., Slavney S., Smith M., Shyong W.J.,
50 1220 Strohbehn K., Taylor H., Thompson P., Tossman B., Wirzburger M., and Wolff M. 2007.
51 1221 Compact reconnaissance imaging spectrometer for Mars (CRISM) on Mars
52 1222 reconnaissance orbiter (MRO). Journal of Geophysical Research: Planets, 112(E5S03).

- 1
2
3 1223 Muttik N., Kirsimaee K., Somelar P., and Osinski G.R. 2008. Post-impact alteration of surficial
4 1224 suevites in Ries crater, Germany: Hydrothermal modification or weathering processes?
5 1225 Meteoritics & Planetary Science, 43(11), pp.1827-1840.
- 7 1226 Nachon M., Clegg S.M., Mangold N., Schröder S., Kah L.C., Dromart G., Ollila A., Johnson
8 1227 J.R., Oehler D.Z., Bridges J.C., Le Mouélic S., Forni O., Wiens R.C., Anderson R.B.,
9 1228 Blaney D.L., Bell III J.F., Clark B., Cousin A., Dyar M.D., Ehlmann B., Fabre C.,
10 1229 Gasnault O., Grotzinger J., Lasue J., Lewin E., Léveillé R., McLennan S., Meslin P.-Y.,
11 1230 Rapin W., Rice M., Squyres S.W., Stack K., Sumner D.Y., Vaniman D., and Wellington
12 1231 D. 2014. Calcium sulfate veins characterized by ChemCam/Curiosity at Gale crater,
13 1232 Mars. *Journal of Geophysical Research: Planets*, 119(9), 1991-2016.
- 15 1233 Olsson-Francis K., Pearson V.K., Steer E.D., and Schwenzer S.P. 2017. Determination of
16 1234 Geochemical Bio-Signatures in Mars-Like Basaltic Environments. *Frontiers in*
17 1235 *Microbiology*, 8: article no. 1668.
- 19 1236 Osinski G.R., Tornabene L.L., Banerjee N.R., Cockell C.S., Flemming R., Izawa M.R.,
20 1237 McCutcheon J., Parnell J., Preston L.J., Pickersgill A.E., Pontefact A., Sapers H.M., and
21 1238 Southam G. 2013. Impact-generated hydrothermal systems on Earth and Mars. *Icarus*,
22 1239 224(2), pp.347-363.
- 24 1240 Palandri J.L. and Reed M.H. 2004. Geochemical models of metasomatism in ultramafic systems:
25 1241 serpentinization, rodingitization, and sea floor carbonate chimney precipitation.
26 1242 *Geochimica et Cosmochimica Acta*, 68(5), 1115-1133.
- 28 1243 Peng Z.X., Mahoney J.J., Hooper P.R., Macdougall J.D., and Krishnamurthy P. 1998. Basalts of
29 1244 the northeastern Deccan Traps, India: isotopic and elemental geochemistry and relation to
30 1245 southwestern Deccan stratigraphy. *Journal of Geophysical Research: Solid Earth*,
31 1246 103(B12), pp.29843-29865.
- 33 1247 Peretyazhko T.S., Fox A., Sutter B., Niles P.B., Adams M., Morris R.V., and Ming D.W. 2016.
34 1248 Synthesis of akaganeite in the presence of sulfate: Implications for akaganeite formation
35 1249 in Yellowknife Bay, Gale Crater, Mars. *Geochimica et Cosmochimica Acta*, 188, 284-
36 1250 296.
- 38 1251 Peretyazhko T.S., Ming D.W., Rampe E.B., Morris R.V., and Agresti D.G. 2018. Effect of
39 1252 solution pH and chloride concentration on akaganeite precipitation: Implications for
40 1253 akaganeite formation on Mars. *Journal of Geophysical Research: Planets*, 123(8), 2211-
41 1254 2222.
- 43 1255 Pinckney L.R. and Burnham C.W. 1988. Effects of compositional variation on the crystal
44 1256 structures of pyroxmangite and rhodonite. *American Mineralogist*, 73(7-8), 798-808.
- 46 1257 Rampe E.B., Ming D.W., Blake D.F., Bristow T.F., Chipera S.J., Grotzinger J.P., Morris R.V.,
47 1258 Morrison S.M., Vaniman D.T., Yen A.S., Achilles C.N., Craig P.I., Des Marais D.J.,
48 1259 Downs R.T., Farmer J.D., Fendrich K.V., Gellert R., Hazen R.M., Kah L.C., Morookian
49 1260 J.M., Peretyazhko T.S., Sarrazin P., Treiman A.H., Berger J.A., Eigenbrode J., Fairén
50 1261 A.G., Forni O., Gupta S., Hurowitz J.A., Lanza N.L., Schmidt M.E., Siebach K., Sutter
51 1262 B., and Thompson L.M. 2017. Mineralogy of an ancient lacustrine mudstone succession
52 1263 from the Murray formation, Gale crater, Mars. *Earth and Planetary Science Letters*, 471,
53 1264 172-185.

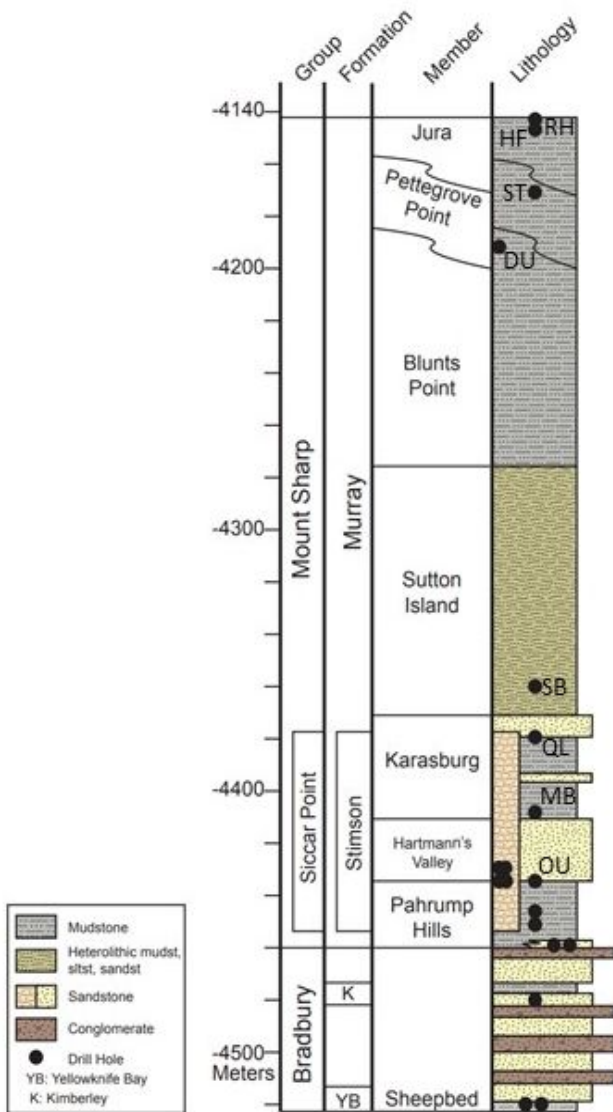
- 1
2
3 1265 Rampe E.B., Blake D.F., Bristow T.F., Ming D.W., Vaniman D.T., Morris R.V., Achilles C.N.,
4 1266 Chipera S.J., Morrison S.M., Tu V.M., Yen A.S., Castle N., Downs G.W., Downs R.T.,
5 1267 Grotzinger J.P., Hazen R.M., Treiman A.H., Peretyazhko T.S., Des Marais D.J., Walroth
6 1268 R.C., Craig P.I., Crisp J.C., Lafuente B., Morookian J.M., Sarrazin P.C., Thorpe M.T.,
7 1269 Bridges J.C., Edgar L.A., Fedo C.M., Freissinet C., Gellert R., Mahaffy P.R., Newsom
8 1270 H.E., Johnson J.R., Kah L.C., Siebach K.L., Schieber J., Sun V.Z., Vasavada A.R.,
9 1271 Wellington D., Wiens R.C., and the MSL Science Team 2020a. Mineralogy and
10 1272 Geochemistry of Sedimentary Rocks and Eolian Sediments in Gale Crater, Mars: A
11 1273 Review after Six Earth Years of Exploration with *Curiosity*. *Geochemistry*, 80(2),
12 1274 125605, doi: 10.1016/j.chemer.2020.125605.
- 15 1275 Rampe E.B., Bristow T.F., Morris R.V., Morrison S.M., Achilles C.N., Ming D.W., Vaniman
16 1276 D.T., Blake D.F., Tu V.M., Chipera S.J., Yen A.S., Peretyazhko T.S., Downs R.T., Hazen
17 1277 R.M., Treiman A.H., Grotzinger J.P., Castle N., Craig P.I., Des Marais D.J., Thorpe
18 1278 M.T., Walroth R.C., Downs G.W., Fraeman A.A., Siebach K.L., Gellert R., Lafuente B.,
19 1279 McAdam A.C., Meslin P.-Y., Sutter B., and Salvatore M.R. 2020b. Mineralogy of Vera
20 1280 Rubin ridge from the Mars Science Laboratory CheMin instrument. *Journal of*
21 1281 *Geophysical Research: Planets*, 125, e2019E006306.
- 24 1282 Rapin W., Ehlmann B.L., Dromart G., Schieber J., Thomas N.H., Fischer W.W., Fox V.K., Stein
25 1283 N.T., Nachon M., Clark B.C., Kah L.C., Thompson L., Meyer H.A., Gabriel T.S.J.,
26 1284 Hardgrove C., Mangold N., Rivera-Hernandez F., Wiens R.C., and Vasavada A.R. 2019.
27 1285 An interval of high salinity in ancient Gale crater lake on Mars. *Nature Geoscience*, 12,
28 1286 889-895.
- 30 1287 Reed M.H. 1983. Seawater-basalt reaction and the origin of greenstones and related ore deposits.
31 1288 *Economic Geology*, 78(3), 466-485.
- 33 1289 Reed M.H. 1997. Hydrothermal alteration and its relationship to ore fluid composition. In:
34 1290 Barnes, H.L. (Ed.), *Geochemistry of Hydrothermal Ore Deposits*, third ed. John Wiley &
35 1291 Sons, New York, pp. 303-365.
- 37 1292 Reed M.H., Spycher N.F., and Palandri J. 2010. User Guide for CHIM-XPT: A Program for
38 1293 Computing Reaction Processes in Aqueous-Mineral-Gas Systems and MINTAB Guide.
39 1294 71p., University of Oregon, Eugene.
- 41 1295 Rimstidt J.D. 2014. *Geochemical Rate Models. An Introduction to Geochemical Kinetics*.
42 1296 Cambridge University Press, New York, 232p.
- 43 1297 Rivera-Hernandez F., Sumner D.Y., Mangold N., Stack K.M., Edgett K.S., Bennett K.A., Wiens
44 1298 R.C., Sun V.Z., Heydari E., and Maurice S. 2019. Vera Rubin Ridge (Gale Crater, Mars)
45 1299 Grain Size Observations from ChemCam LIBS Data, and Interpretations. In *Proceedings*
46 1300 *Lunar and Planetary Science Conference, The Woodlands, TX (Vol. 50, p. 3029)*.
- 48 1301 Robinson D., and Bevins R.E. 1999. Patterns of regional low-grade metamorphism in
49 1302 metabasites, in *Low-Grade Metamorphism*, edited by M. Frey and D. Robinson, pp. 143-
50 1303 168, Blackwell Sci, Oxford, U.K.
- 52 1304 Salil M.S., Shrivastava J.P., and Pattanayak S.K. 1997. Similarities in the mineralogical and
53 1305 geochemical attributes of detrital clays of Maastrichtian Lameta Beds and weathered
54 1306 Deccan basalt, Central India. *Chemical Geology*, 136(1-2), pp.25-32.

- 1
2
3 1307 Sapers H. M., Osinski G. R., Flemming R. L., Buitenhuis E., Banerjee N. R., Tornabene L. L.,
4 1308 Blain S., and Hainge J. 2017. Evidence for a spatially extensive hydrothermal system at
5 1309 the Ries impact structure, Germany. *Meteoritics & Planetary Science* 52:351–371.
- 7 1310 Schieber J., Bish D., Coleman M., Reed M., Hausrath E.M., Cosgrove J., Gupta S., Minitti M.E.,
8 1311 Edgett K.S., and Malin M. 2017. Encounters with an unearthy mudstone: Understanding
9 1312 the first mudstone found on Mars. *Sedimentology*, 64, 311-358. doi:10.1111/sed.12318.
- 11 1313 Schmiieder M., Kennedy T., Jourdan F., Buchner E., and Reimold W.U. 2018. A high-precision
12 1314 $^{40}\text{Ar}/^{39}\text{Ar}$ age for the Nördlinger Ries impact crater, Germany, and implications for the
13 1315 accurate dating of terrestrial impact events. *Geochimica et Cosmochimica Acta*, 220,
14 1316 pp.146-157.
- 16 1317 Schwenzer S.P. and Kring D.A. 2009. Impact-generated hydrothermal systems capable of
17 1318 forming phyllosilicates on Noachian Mars. *Geology*, 37(12), 1091-1094.
- 19 1319 Schwenzer S.P. and Kring D.A. 2013. Alteration minerals in impact-generated hydrothermal
20 1320 systems – Exploring host rock variability *Icarus*, 226, 487-496.
- 22 1321 Schwenzer S.P., Abramov O., Allen C.C., Bridges J.C., Clifford S.M., Filiberto J., Kring D.A.,
23 1322 Lasue J., McGovern P.J., Newsom H.E., Treiman A.H., Vaniman D.T., Wiens R.C., and
24 1323 Wittmann A. 2012. Gale Crater: Formation and post-impact hydrous environments.
25 1324 *Planetary and Space Science*, 70(1), 84-95.
- 27 1325 Schwenzer S.P., Bridges J.C., Wiens R.C., Conrad P.G., Kelley S.P., Leveille R., Mangold N.,
28 1326 Martin-Torres J., McAdam A., Newsom H., Zorzano M.P., Rapin W., Spray J., Treiman
29 1327 A.H., Westall F., Fairén A.G., and Meslin P.-Y. 2016. Fluids during diagenesis and
30 1328 sulfate vein formation in sediments at Gale crater, Mars. *Meteoritics & Planetary
31 1329 Science*, 51(11), 2175-2202. doi: 10.1111/maps.12668.
- 33 1330 Schwertmann U. and Murad E. 1983. Effect of pH on the formation of goethite and hematite
34 1331 from ferrihydrite. *Clays and Clay Minerals*, 31(4), pp.277-284.
- 36 1332 Smith R.J., Dehouck E., and McLennan S. 2019. Amorphous Component Compositional Ranges
37 1333 in Gale Crater, Mars. Ninth International Conference on Mars, abstract #6324.
- 39 1334 Stack K.M., Grotzinger J.P., Lamb M.P., Gupta S., Rubin D.M., Kah L.C., Edgar L.A., Fey
40 1335 D.A., Hurowitz J.A., McBride M., Rivera-Hernandez F., Sumner D.Y., van Beek J.K.,
41 1336 Williams R.M.E., and Yingst R.A. 2019. Evidence for plunging river plume deposits in
42 1337 the Pahrump Hills member of the Murray formation, Gale crater, Mars. *Sedimentology*,
43 1338 66(5), 1768-1802.
- 45 1339 Stein N., Grotzinger J.P., Schieber J., Mangold N., Hallet B., Newsom H., Stack K.M., Berger
46 1340 J.A., Thompson L., Siebach K.L., Cousin A., Le Mouélic S., Minitti M., Sumner D.Y.,
47 1341 Fedo C., House C.H., Gupta S., Vasavada A.R., Gellert R., Wiens R.C., Frydenvang J.,
48 1342 Forni O., Meslin P.Y., Payré V., and Dehouck E. 2018. Desiccation cracks provide
49 1343 evidence of lake drying on Mars, Sutton Island member, Murray formation, Gale Crater.
50 1344 *Geology*, 46(6), 515-518.
- 52 1345 Sutter B., Mcadam A.C., Mahaffy P.R., Ming D.W., Edgett K.S., Rampe E.B., Eigenbrode J.L.,
53 1346 Franz H.B., Freissinet C., Grotzinger J.P., Steele A., House C.H., Archer P.D., Malespin
54 1347 C.A., Navarro-González R., Stern J.C., Bell J.F., Calef F.J., Gellert R., Glavin D.P.,
55 1348 Thompson L.M., and Yen A.S. 2017. Evolved gas analyses of sedimentary rocks and
56
57
58
59
60

- 1
2
3 1349 eolian sediment in Gale Crater, Mars: Results of the Curiosity rover's sample analysis at
4 1350 Mars instrument from Yellowknife Bay to the Namib Dune. *Journal of Geophysical*
5 1351 *Research: Planets*, 122(12), 2574-2609.
- 7 1352 Tantawy M.A., Shatat M.R., El-Roudi A.M., Taher M.A., and Abd-El-Hamed M. 2014. Low
8 1353 temperature synthesis of belite cement based on silica fume and lime. *International*
9 1354 *scholarly research notices*, 2014.
- 11 1355 Thompson L.M., Berger J.A., Spray J.G., Fraeman A.A., McCraig M.A., O'Connell-Cooper
12 1356 C.D., Schmidt M.E., VanBommel S., Gellert R., Yen A., and Boyd N.I. 2020. APXS-
13 1357 Derived Compositional Characteristics of Vera Rubin Ridge and Murray Formation, Gale
14 1358 Crater, Mars: Geochemical Implications for the Origin of the Ridge. *Journal of*
15 1359 *Geophysical Research: Planets*, 125, e2019JE006319.
- 17 1360 Tosca N.J., McLennan S.M., Dyar M.D., Sklute E.C., and Michel F.M. 2008. Fe oxidation
18 1361 processes at Meridiani Planum and implications for secondary Fe mineralogy on Mars.
19 1362 *Journal of Geophysical Research*, **113**: doi: 10.1029/2007JE003019.
- 21 1363 Tosca N.J., McLennan S.M., Lindsley D.H., and Schoonen M.H. 2004. Acid-sulfate weathering
22 1364 of synthetic Martian basalt: The acid fog model revisited. *Journal of Geophysical*
23 1365 *Research*, **109**: E 05003, doi: 10.1029/2003JE002218, 29 p.
- 25 1366 Treiman A.H., and Essene E.J. 1983. Phase equilibria in the system CaO-SiO₂-CO₂. *American*
26 1367 *Journal of Science A*, 283, 97-120.
- 28 1368 Treiman A.H., Morris R.V., Agresti D.G., Graff T.G., Achilles C.N., Rampe E.B., Bristow T.F.,
29 1369 Ming D.W., Blake D.F., Vaniman D.T., Bish D.L., Chipera S.J., Morrison S.M., and
30 1370 Downs R.T. 2014. Ferrian saponite from the Santa Monica Mountains (California, USA,
31 1371 Earth): Characterization as an analog for clay minerals on Mars with application to
32 1372 Yellowknife Bay in Gale Crater. *American Mineralogist*, 99(11-12), 2234-2250,
33 1373 <http://dx.doi.org/10.2138/am-2014-4763>.
- 35 1374 Turner S.M.R., Schwenger S.P., Bridges J.C., Bedford C.C., Rampe E.B., Fraeman A.A.,
36 1375 McAdam A., Mangold N., and L'Haridon J. 2019. Thermochemical Modelling of Fluid-
37 1376 Rock Reactions in Vera Rubin ridge, Gale crater, Mars. In *Lunar and Planetary Science*
38 1377 *Conference (Vol. 50, p. 1897)*.
- 40 1378 Vaniman D.T., Bish D.L., Ming D.W., Bristow T.F., Morris R.V., Blake D.F., Chipera S.J.,
41 1379 Morrison S.M., Treiman A.H., Rampe E.B., Rice M., Achilles C.N., Grotzinger J.P.,
42 1380 McLennan M., Williams J., Bell III J.F., Newsom H.E., Downs R.T., Maurice S.,
43 1381 Sarrazin P., Yen A.S., Morookian J.M., Farmer J.D., Stack K., Milliken R.E., Ehlmann
44 1382 B.L., Sumner D.Y., Berger G., Crisp J.A., Hurowitz J.A., Anderson R., Des Marais D.J.,
45 1383 Stolper E.M., Edgett K.S., Gupta S., Spanovich N., and the MSL Science Team 2014.
46 1384 Mineralogy of a mudstone at Yellowknife Bay, Gale crater, Mars. *Science*, 343(6169),
47 1385 p.1243480.
- 50 1386 Varnes E.S., Jakorsky B.M., and McCollom T.M. 2003. Biological Potential of martian
51 1387 Hydrothermal Systems. *Astrobiology*, **3**: 407-414.
- 53 1388 Vernié P., Kienast J.R. and Mével C. 1986. The occurrence of deerite in highly oxidizing
54 1389 conditions within the 'schistes lustrés' of eastern Corsica. *Journal of Metamorphic*
55 1390 *Geology*, 4(4), 385-399.

- 1
2
3 1391 von Engelhardt W. 1997. Suevite breccia of the Ries impact crater, Germany: Petrography,
4 1392 chemistry and shock metamorphism of crystalline rock clasts. *Meteoritics & Planetary*
5 1393 *Science*, 32(4), pp.545-554.
- 7 1394 Williams R.M.E., Grotzinger J.P., Dietrich W.E., Gupta S., Sumner D.Y., Wiens R.C., Mangold
8 1395 N., Malin M.C., Edgett K.S., Maurice S., Forni O., Gasnault O., Ollila A., Newsom H.E.,
9 1396 Dromart G., Palucis M.C., Yingst R.A., Anderson R.B., Herkenhoff K.E., Le Mouélic S.,
10 1397 Goetz W., Madsen M.B., Koefoed A., Jensen J.K., Bridges J.C., Schwenzer S.P., Lewis
11 1398 K.W., Stack K.M., Rubin D., Kah L.C., Bell III J.F., Farmer J.D., Sullivan R., Van Beek
12 1399 T., Blaney D.L., Pariser O., Deen R.G., and the MSL Science Team 2013. Martian fluvial
14 1400 conglomerates at Gale crater. *science*, 340(6136), pp.1068-1072.
- 16 1401 Wong G.M., Lewis J.M.T., Knudson C.A., Millan M., McAdam A.C., Eigenbrode J.L.,
17 1402 Andrejkovičová S., Gómez F., Navarro-González R., and House C.H. 2020. Detection of
18 1403 Reduced Sulfur on Vera Rubin Ridge by Quadratic Discriminant Analysis of Volatiles
19 1404 Observed During Evolved Gas Analysis. *Journal of Geophysical Research: Planets*, 125,
20 1405 e2019JE006304.
- 22 1406 Zolotov M.Y. and Mironenko M.V. 2007. Timing of acid weathering on mars: A kinetic-
23 1407 thermodynamic assessment. *Journal of Geophysical Research*, **112**: doi:
24 1408 10.1029/2006JE002882, 20p.
- 26 1409 Zolotov M.Y. and Mironenko M.V. 2016. Chemical models for martian weathering profiles:
27 1410 Insights into formation of layered phyllosilicate and sulfate deposits. *Icarus*, 275. 203-
28 1411 220.
- 30 1412 Zolotov M.Y. and Shock E.L. 1999. Abiotic synthesis of polycyclic aromatic hydrocarbons on
31 1413 Mars. *Journal of Geophysical Research*, **104**: 14033–14049.
- 33 1414 Zolotov M.Y. and Shock E.L. 2005. Formation of jarosite-bearing deposits through aqueous
34 1415 oxidation of pyrite at Meridani Planum, Mars. *Geophysical Research Letters*, **32**: doi:
35 1416 10.1029/2005GL024253, 5 p.

1417 Figures and Tables



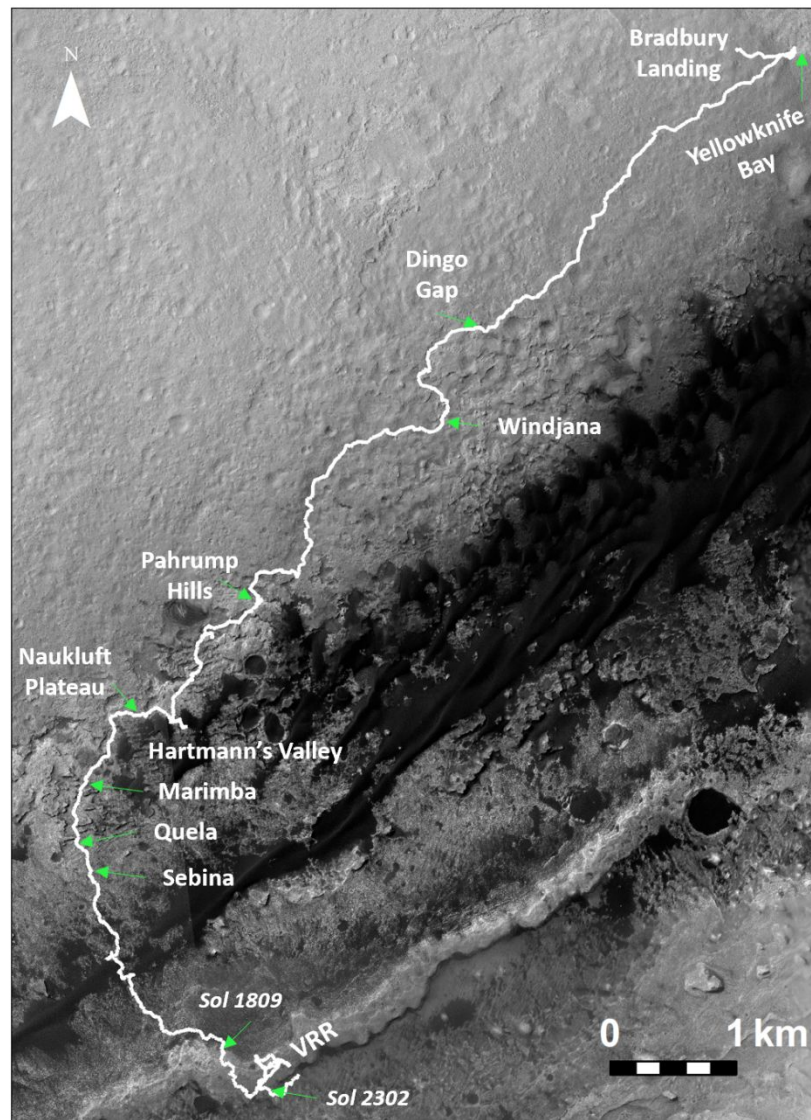
1418

1419 Fig. 1. Stratigraphic column detailing the morphological characteristics of the stratigraphic
 1420 groups and units encountered by the *Curiosity* rover up to and including the Jura member. Drill
 1421 holes of interest in this study are annotated: Oudam (OU), Marimba (MB), Quela (QL), Sebina
 1422 (SB), Duluth (DU), Stoer (ST), Highfield (HF), and Rock Hall (RH). Image credit: The MSL
 1423 sedimentology and stratigraphy working group.

1424

1425

1426



1427

1428

1429

1430

1431

1432

1433

1434

1435

1436

1437

1438

1439

1440

1441

1442

1443

1444

1445

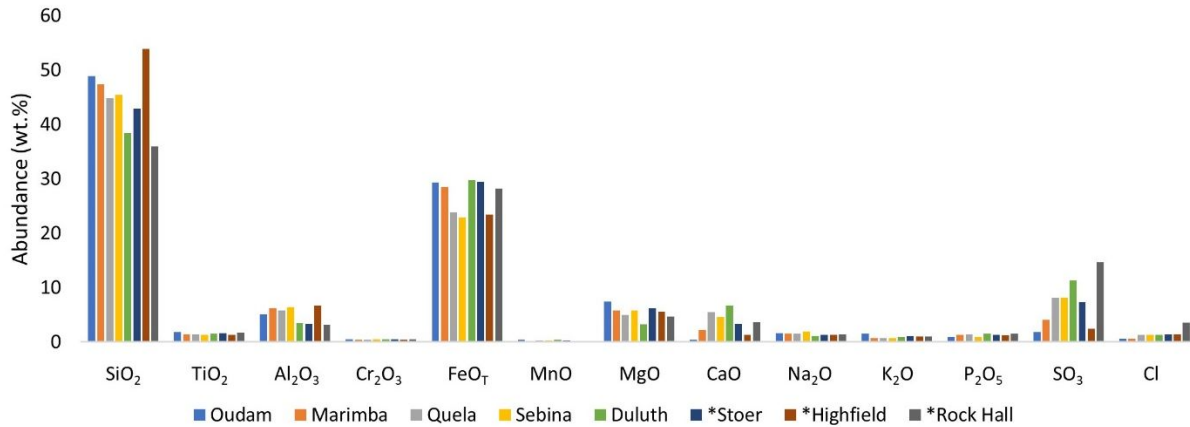
Fig. 2. HiRISE orbital overview of the NASA Mars Science Laboratory *Curiosity* rover's traverse from Bradbury Landing up to sol 2359. Select locations are annotated as well as sol 1809 when *Curiosity* ascended on to Vera Rubin ridge (VRR), and sol 2302 when *Curiosity* traversed off VRR and into the Clay Bearing Unit. Adapted image from NASA-JPL/Fraeman.

1
2
3 1434 Table 1. Ratio of alteration to primary mineral content per drill hole, including and excluding
4 1435 amorphous component as an alteration component. Ca-sulfates were excluded. Errors propagated
5 1436 from uncertainty in CheMin mineral abundances. Pyroxenes and feldspars were considered to be
6 1437 primary minerals. Fe-oxides, jarosite, quartz, halite, fluorapatite and phyllosilicates were
7 1438 considered to be alteration. Source data take from Achilles et al. (2020) and Rampe et al.
8 1439 (2020b).

Drill hole	Including Amorphous	Excluding Amorphous
Oudam	2.1 ± 0.4	0.6 ± 0.1
Marimba	4.9 ± 0.8	2.3 ± 0.3
Quela	4.1 ± 0.8	1.3 ± 0.1
Sebina	5.3 ± 1.0	1.8 ± 0.2
Duluth	2.9 ± 0.3	0.8 ± 0.3
Stoer	2.3 ± 0.2	1.0 ± 0.2
Highfield	2.5 ± 0.2	0.6 ± 0.1
Rock Hall	2.0 ± 0.6	0.9 ± 0.2

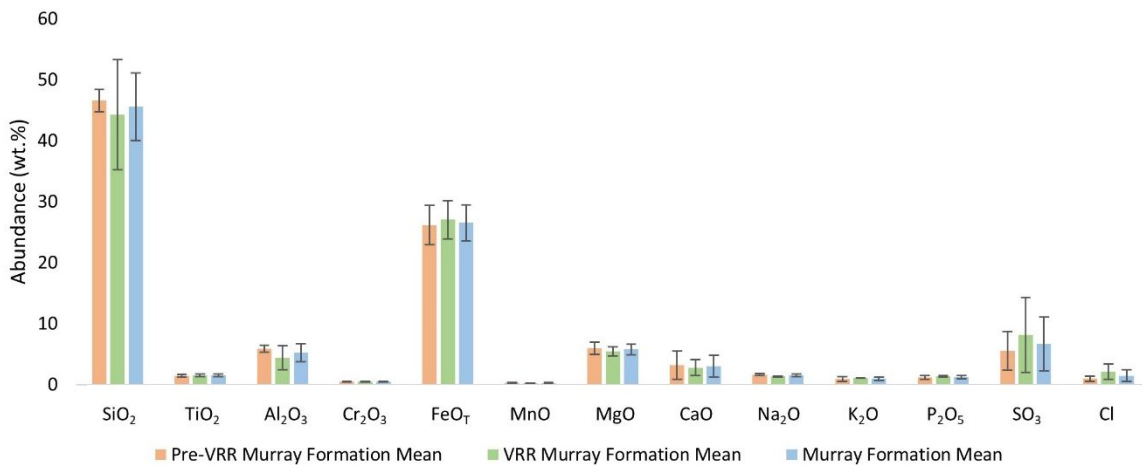
1440

1441



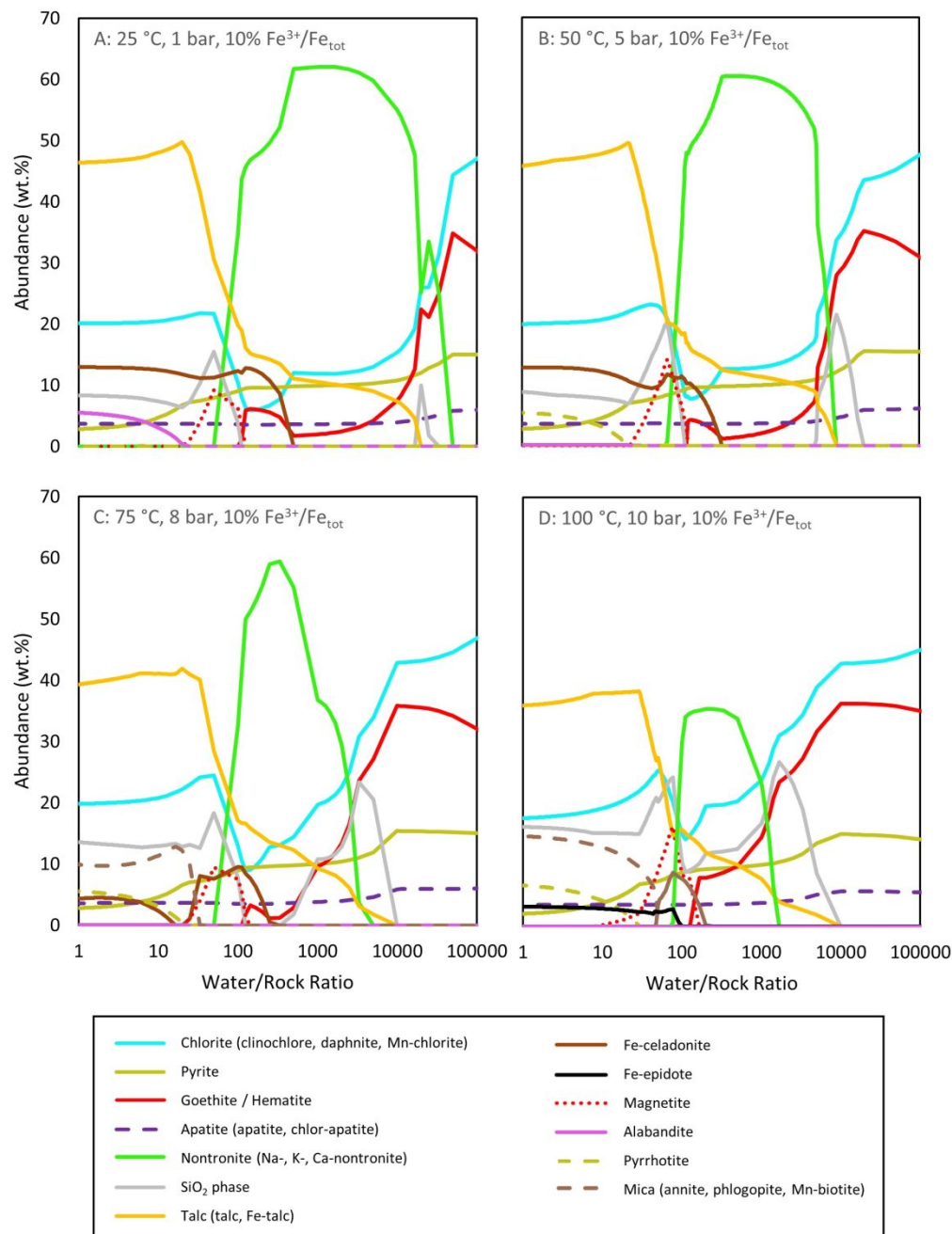
1442

1443 Fig. 3. Main-phase alteration assemblage compositions for Oudam, Marimba, Quela, Sebina,
 1444 Duluth, Stoer, Highfield and Rock Hall. Calculated using APXS and CheMin results (Achilles et
 1445 al., 2020; Rampe et al., 2020b), as explained in hypothesis and model set-up section “Host Rock
 1446 Composition”. Samples Oudam, Marimba, Quela, Sebina, and Duluth are from pre-VRR Murray
 1447 formation localities. Stoer, Highfield and Rock Hall represent VRR Murray. *indicates drill
 1448 samples acquired from VRR.
 1449



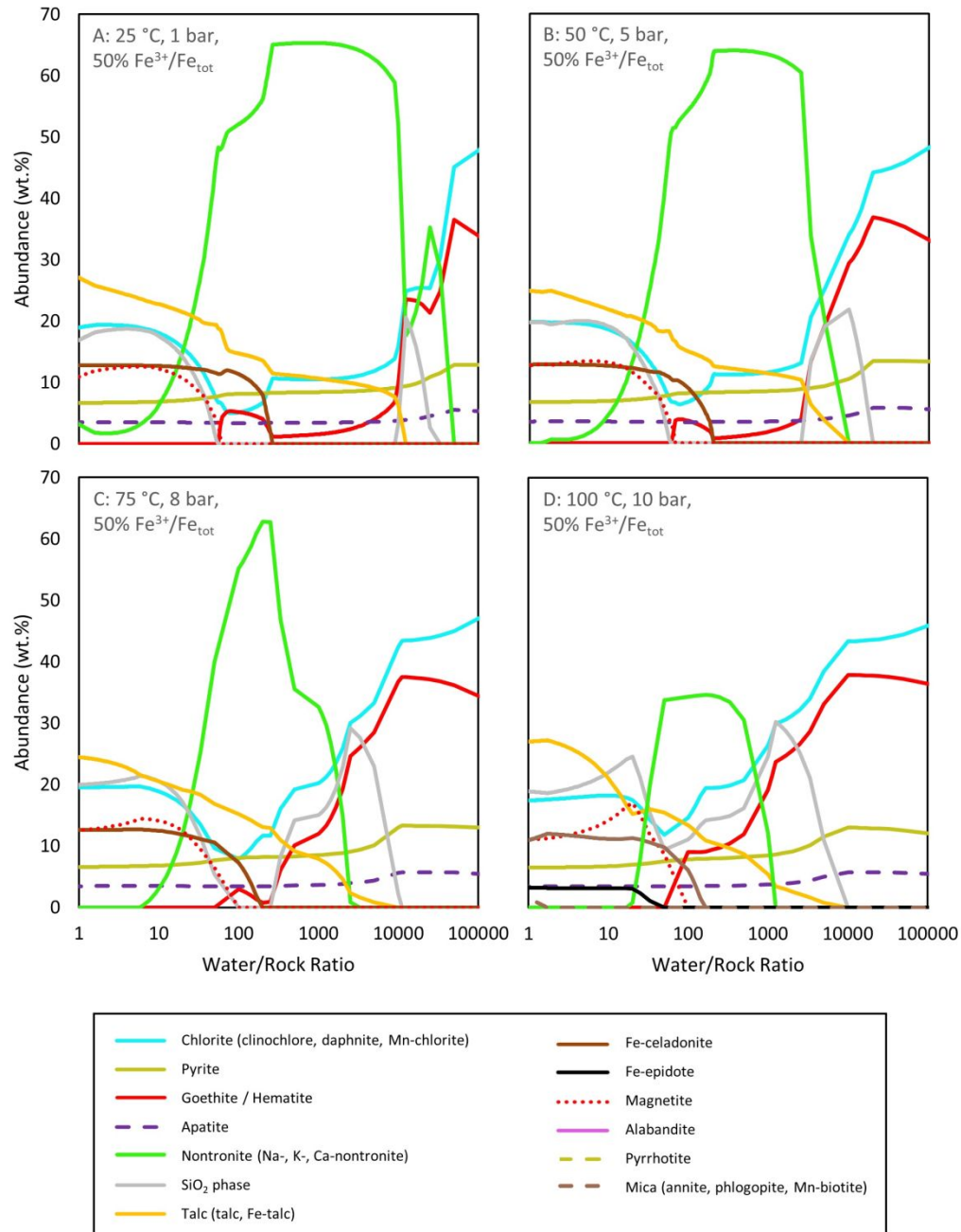
1450

1451 Fig. 4. Mean alteration compositions for the Pre-VRR Murray formation (Oudam, Marimba,
 1452 Quela, Sebina), VRR Murray Formation (Stoer, Highfield and Rock Hall), the overall Murray
 1453 Formation. Calculated using APXS and CheMin results. Error bars show standard deviation for
 1454 each calculated mean, illustrating the statistical similarity between the calculated alteration
 1455 compositions.



1456

1457 Fig. 5. CHIM-XPT results for the calculated VRR alteration composition (Table S4) reacted with
 1458 GPW (Bridges et al., 2015b). Reactions at 25, 50, 75 and 100 °C, and 10% of the FeO_T is Fe³⁺,
 1459 as indicated. Goethite only precipitated at 25 °C (A), and hematite did not precipitate at that
 1460 temperature. K-nontronite precipitated at 25 °C (A), whereas Na-nontronite did not precipitate at
 1461 100 °C (D) and Ca-nontronite precipitated at all temperatures. Chlor-apatite formed at 25 °C (A),
 1462 50 °C (B) and 75 °C (C), whereas apatite formed at 75 °C (C) and 100 °C (D). Trace abundances
 1463 of calcite, spurrite and merwinite are not included on the plots.



1464

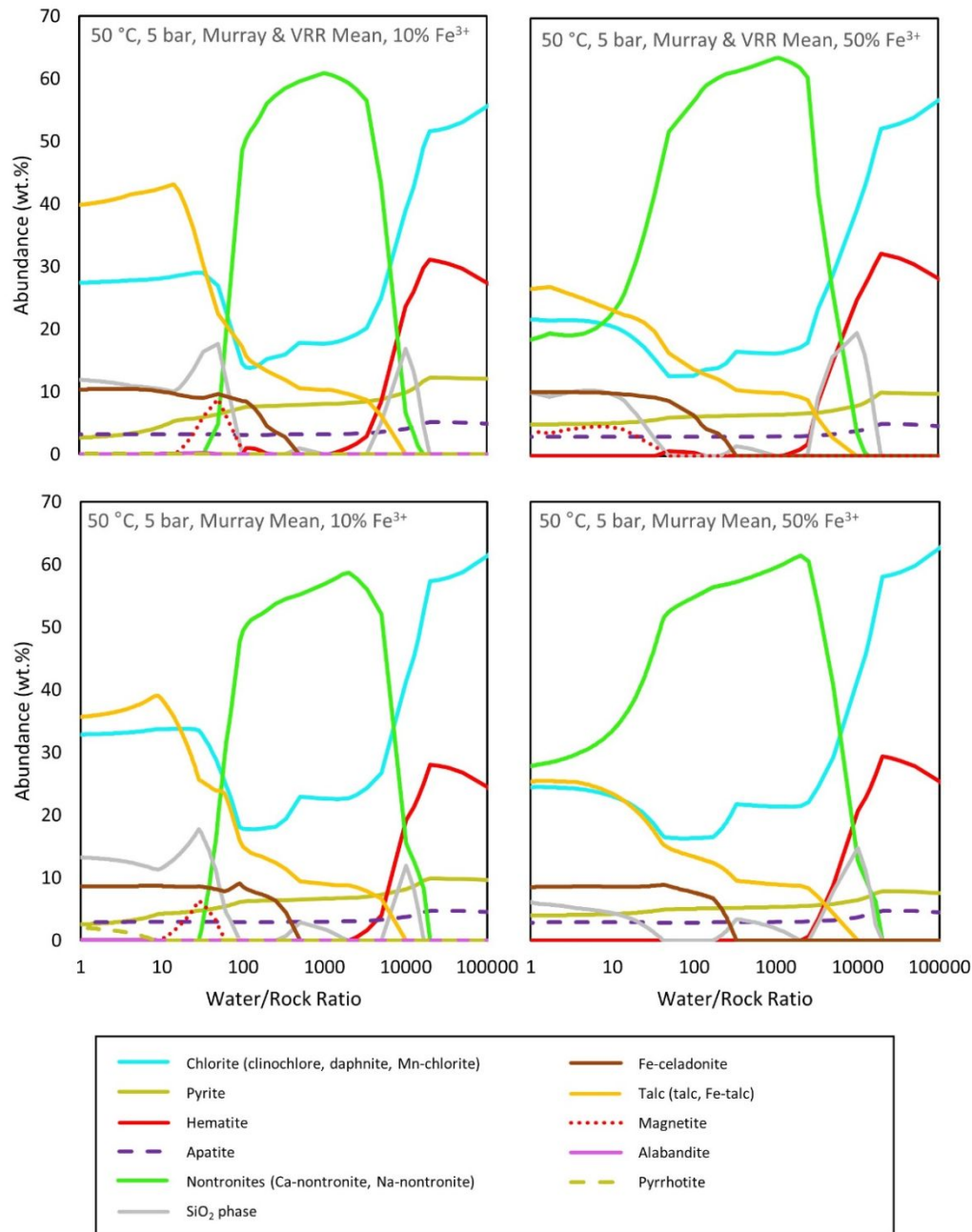
1465 Fig. 6. CHIM-XPT results for the calculated VRR alteration composition (Table S4) reacted with
 1466 GPW (Bridges et al., 2015b). Reactions at 25, 50, 75 and 100 °C, and 50% of the FeO_T is Fe³⁺,
 1467 as indicated. Goethite only precipitated at 25 °C (A), and hematite did not precipitate at that
 1468 temperature. K-nontronite precipitated at 25 °C (A) and 50°C (B), whereas Na-nontronite did not
 1469 precipitate at 100 °C (D) and Ca-nontronite precipitated at all temperatures. Rhodochrosite
 1470 precipitated at 25 °C (A) and 50 °C (B), and trace wt.% of calcite precipitated at all temperatures
 1471 for 50% Fe³⁺/Fe_{tot} (A,B,C,D). Trace abundances of calcite, rhodochrosite, spurrite and merwinite
 1472 are not included on the plots.

1473

1
2
3 1474 Table 2. Summed VRR clay mineral wt.% / Fe-oxide wt.% ratio at high (10,000), intermediate
4 1475 (1,000) and low (100) W/R ratios in thermochemical models (Fig. 6 and 7) using the calculated
5 1476 VRR mean alteration composition (Table S4) as the host rock (at both 10 and 50% Fe³⁺/Fe_{tot})
6 1477 reacted with GPW (Bridges et al., 2015b) at 25, 50, 75 and 100 °C using CHIM-XPT (Reed et
7 1478 al., 2010).

	10% Fe ³⁺ /Fe _{tot} Models			50% Fe ³⁺ /Fe _{tot} Models		
	10,000 W/R	1,000 W/R	100 W/R	10,000 W/R	1,000 W/R	100 W/R
25 °C	10.4	43.2	--	7.7	55.7	13.9
50 °C	1.2	40.7	--	1.2	46.0	21.4
75 °C	1.2	6.9	--	1.2	5.1	26.3
100 °C	1.2	3.8	--	1.1	2.3	6.9

1479

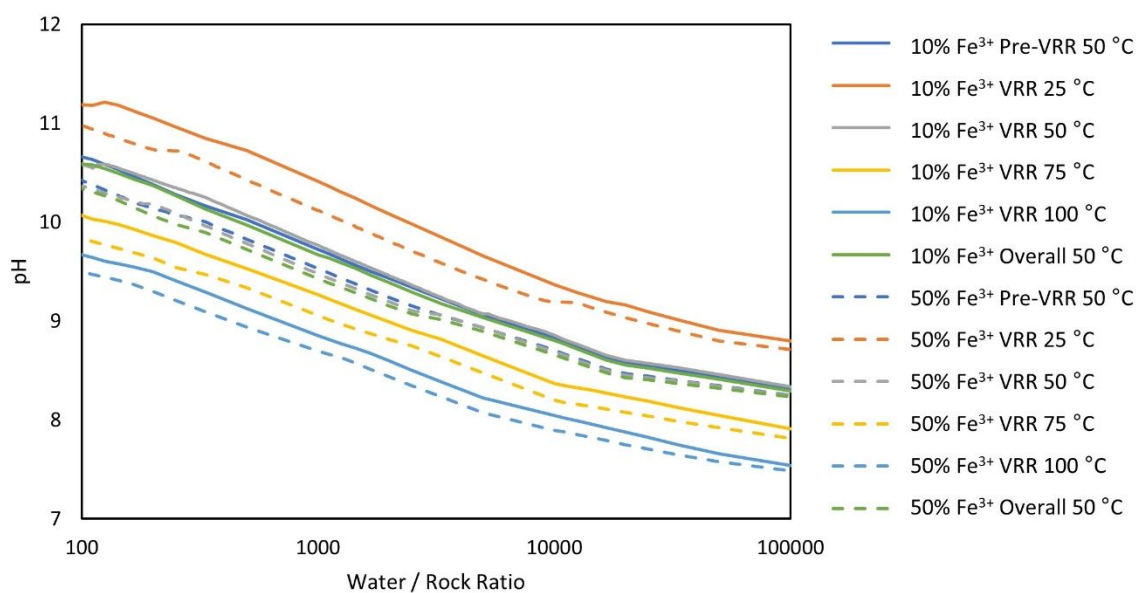


1480

1481 Fig. 7. CHIM-XPT results for the calculated alteration composition for the Murray formation and
 1482 the Murray and VRR (overall) (Table S4) reacted with GPW (Bridges et al., 2015b). Reactions
 1483 are at 50 °C and the Fe³⁺ content of FeO_T is at 10% and 50%, as indicated. Trace abundances of
 1484 rhodochrosite, calcite, spurrite and merwinite are not included on the plot.
 1485

1
2
3 1486 Table 3. Summed clay wt.% / Fe-oxide wt.% ratio at high (10,000), intermediate (1,000) and low
4 1487 (100) W/R ratios in models for the pre-VRR Murray mean and overall mean calculated alteration
5 1488 compositions (Table S4) as the host rock, at 10 and 50% $\text{Fe}^{3+}/\text{Fe}_{\text{tot}}$, reacted with GPW (Bridges
6 1489 et al., 2015b) at 50 °C using CHIM-XPT (Reed et al., 2010).

	10% $\text{Fe}^{3+}/\text{Fe}_{\text{tot}}$ Models			50% $\text{Fe}^{3+}/\text{Fe}_{\text{tot}}$ Models		
	10,000 W/R	1,000 W/R	100 W/R	10,000 W/R	1,000 W/R	100 W/R
Pre-VRR	3.0	--	--	2.6	--	--
Overall	1.9	--	--	1.7	--	--



1492 Fig. 8. Plot showing pH variation with W/R for the CHIM-XPT models shown in Fig. 5 – 7.
1493 Starting compositions for Pre-VRR Murray, VRR Murray and Overall Murray used in the
1494 modeling are shown in Table S4.

Table 4. Calculated clay mineral / hematite and clay mineral / Fe-oxide sum for drilled samples in the pre-VRR Murray formation and VRR, determined using CheMin wt.% mineral abundances (Achilles et al., 2020; Rampe et al., 2020b). Means are included for pre-VRR and VRR samples, as well as an overall mean. Errors shown are propagated errors calculated from errors in mineral abundances.

Drill Hole	Clay mineral / Hematite	Clay mineral / Fe-oxide sum
Oudam	0.3 ± 0.1	0.3 ± 0.1
Marimba	4.4 ± 0.9	4.4 ± 0.9
Quela	2.3 ± 0.4	2.3 ± 0.4
Sebina	2.8 ± 0.6	2.8 ± 0.6
Duluth	2.4 ± 1.1	2.1 ± 1.0
Pre-VRR mean	2.4 ± 0.3	2.4 ± 0.3
Stoer	0.6 ± 0.3	0.6 ± 0.3
Highfield	0.5 ± 0.2	0.5 ± 0.2
Rock Hall	4.5 ± 2.1	1.5 ± 0.7
VRR mean	1.9 ± 0.7	0.8 ± 0.3
Overall mean	2.2 ± 0.3	1.8 ± 0.2

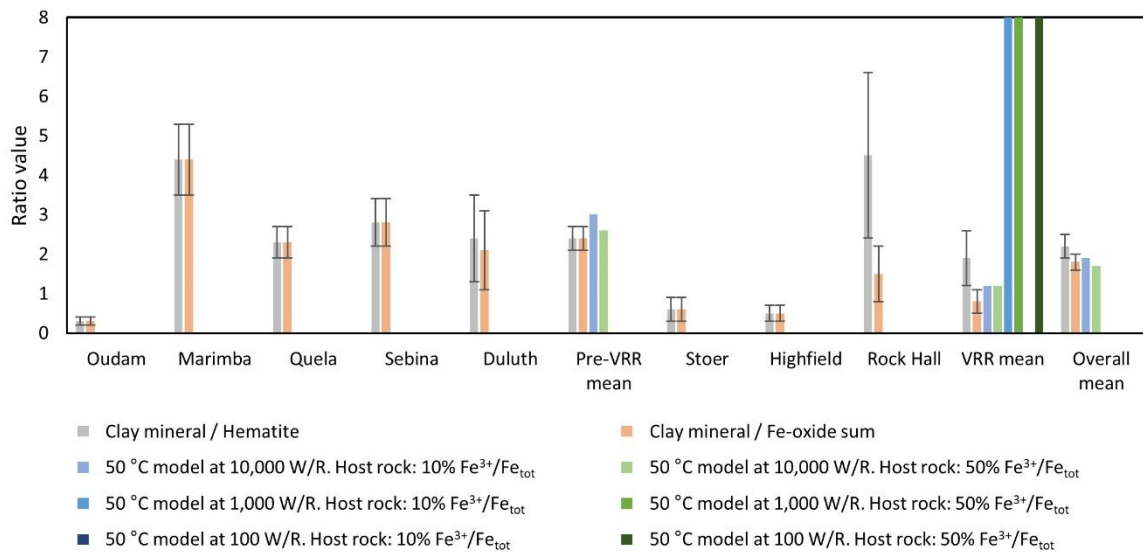
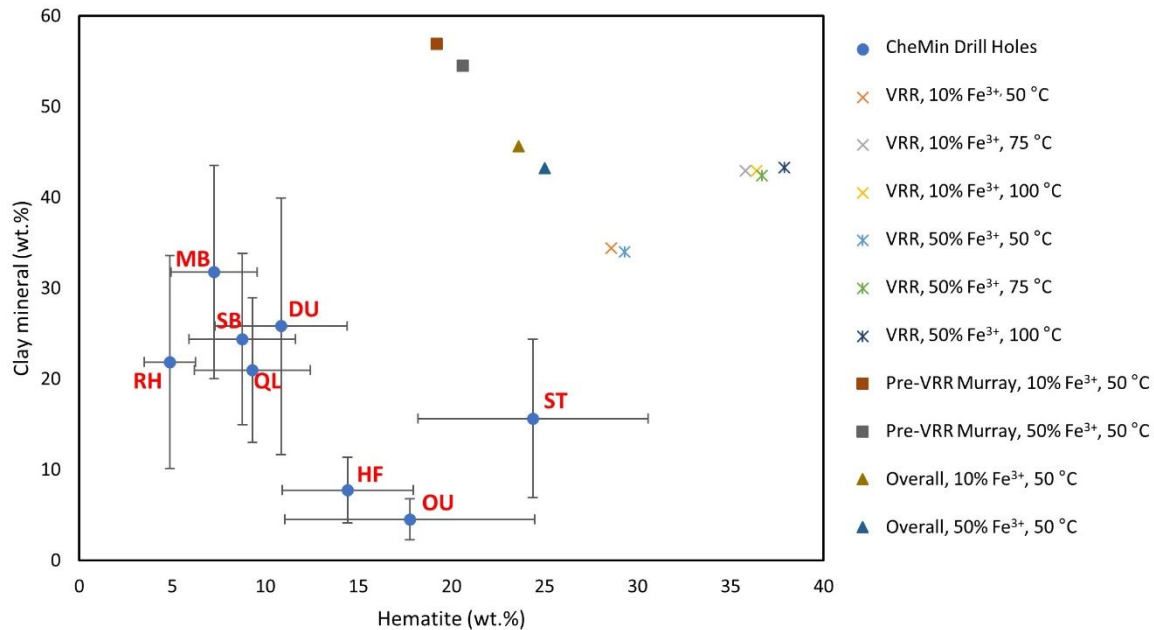
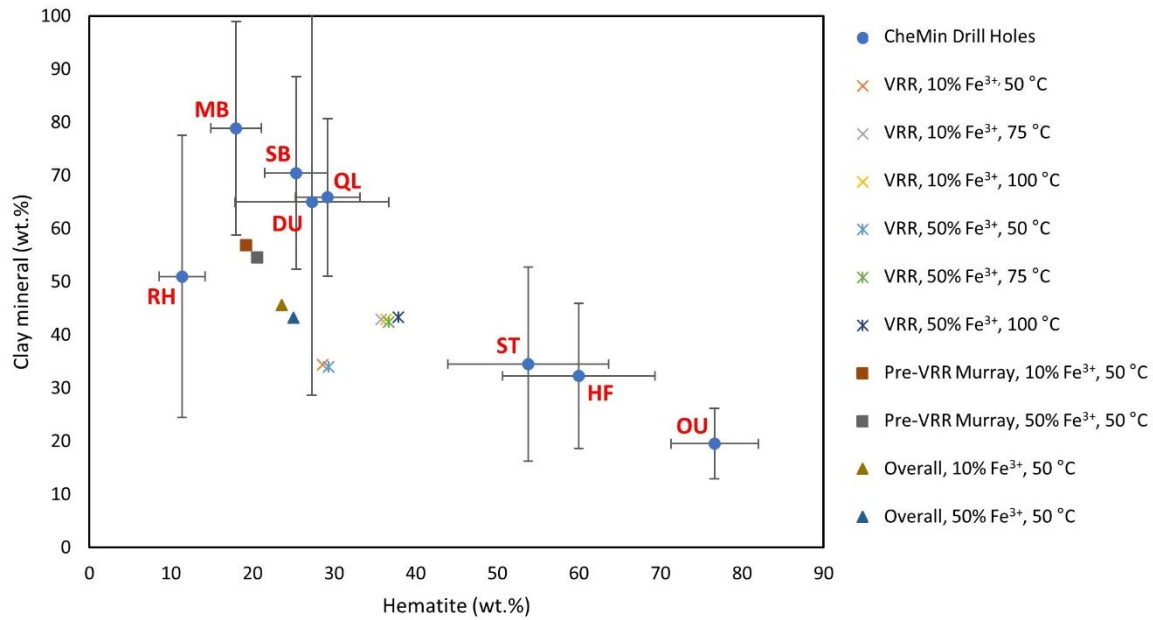


Fig. 9. Plot comparing calculated clay mineral / hematite and clay mineral / Fe-oxide sum for drill samples in the pre-VRR Murray formation and VRR, determined using CheMin wt.% mineral abundances (Achilles et al., 2020; Rampe et al., 2020b). Means are included for pre-VRR and VRR samples, as well as an overall mean. Errors shown are propagated errors calculated from errors in mineral abundances. Values for models run at 50 °C at 10,000 W/R, 1,000 W/R and 100 W/R from Tables 2 and 3 are included for comparison.



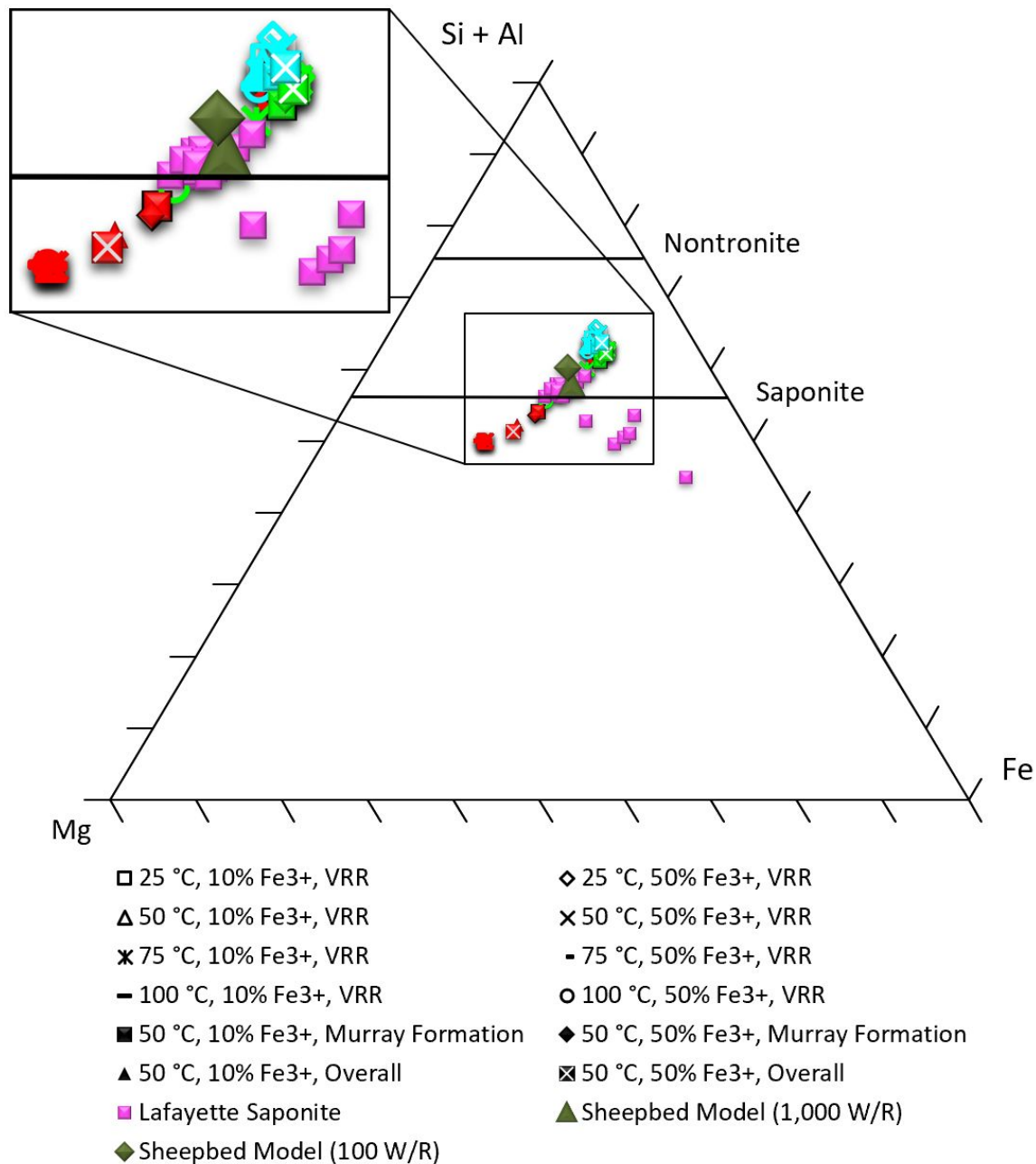
1510

1511 Fig. 10. Clay mineral abundance vs hematite abundance from CheMin (Achilles et al., 2020;
 1512 Rampe et al., 2020b) normalized to the alteration component (including amorphous phase)
 1513 compared to CHIM-XPT results in this study (Figs 5 – 7; Tables S5 and S8) at high (10,000)
 1514 W/R. Drill holes Oudam, Marimba, Quela, Sebina, Duluth, Stoer, Highfield and Rock Hall are
 1515 annotated with OU, MB, QL, SB, DU, ST, HF and RH, respectively. Linear regression carried
 1516 out on thermochemical models at 50 °C in the Fig. revealed the trend
 1517 $y = (-2.35 \pm 0.09)x + (102.15 \pm 2.16)$ with an R^2 value of 0.99. Comparative linear
 1518 regression carried out on CheMin drill samples Oudam, Marimba, Sebina, Quela, Duluth,
 1519 Highfield and Rock Hall in the Fig. gave a trend of $y = (-1.88 \pm 0.56)x + (39.23 \pm 6.24)$
 1520 with an R^2 value of 0.70. This trend changed to $y = (-2.56 \pm 0.45)x + (48.38 \pm 5.33)$ with
 1521 an R^2 value of 0.89 with Rock Hall removed from the analysis.



1522

1523 Fig. 11. Clay mineral abundance vs hematite abundance from CheMin (Achilles et al., 2020;
 1524 Rampe et al., 2020b) normalized to the alteration component (excluding the amorphous
 1525 component) compared to CHIM-XPT results in this study (Fig. 5 – 7; Tables S5 and S8) at high
 1526 (10,000) W/R. The comparable negative correlations of different gradients for the CheMin drill
 1527 holes and the thermochemical models and the trend with temperature shown in Fig. 10 indicates
 1528 that only a part of the derived alteration composition is reactive. Drill hole names and
 1529 abbreviations detailed in Fig. 10 caption.



1531

1532 Fig. 12. Mg-Si+Al-Fe_{tot} at. ternary plot. Results at 10,000 (red), 1,000 (green) and 100 (blue)
 1533 W/R from the thermochemical models in this paper are plotted with some additional data from
 1534 other sources for comparison. Lafayette saponite data taken from Hicks et al. (2014). CHIM-
 1535 XPT results for the Sheepbed unit from Bridges et al. (2015b) at 100 W/R are shown for
 comparison.

1
2
3
4
5
6
7
8
9
10
11
12
13
14
15
16
17
18
19
20
21
22
23
24
25
26
27
28
29
30
31
32
33
34
35
36
37
38
39
40
41
42
43
44
45
46
47
48
49
50
51
52
53
54
55
56
57
58
59
60

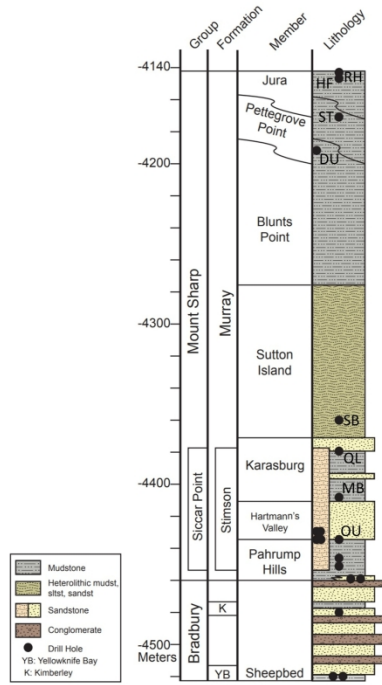


Fig. 1. Stratigraphic column detailing the morphological characteristics of the stratigraphic groups and units encountered by the Curiosity rover up to and including the Jura member. Drill holes of interest in this study are annotated: Oudam (OU), Marimba (MB), Quela (QL), Sebina (SB), Duluth (DU), Stoer (ST), Highfield (HF), and Rock Hall (RH). Image credit: The MSL sedimentology and stratigraphy working group.

190x275mm (300 x 300 DPI)

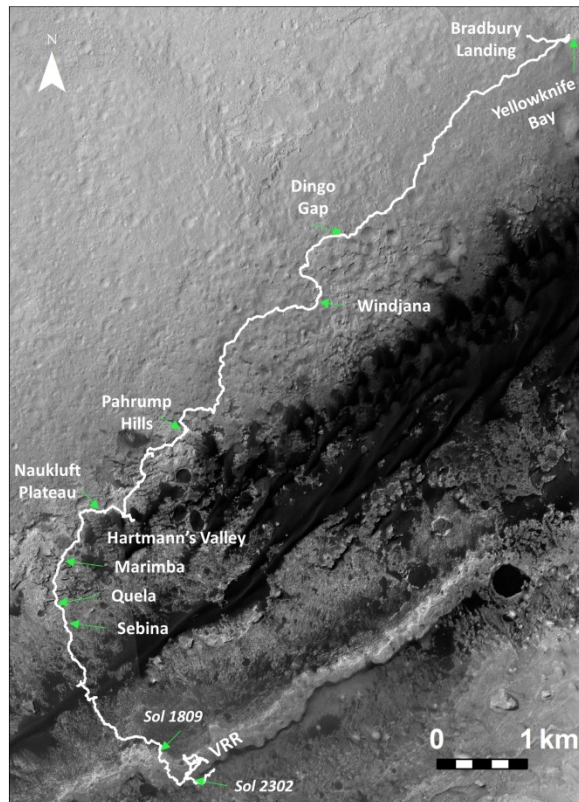
1
2
3
4
5
6
7
8
9
10
11
12
13
14
15
16
17
18
19
20
21
22
23
24
25
26
27
28
29
30
31
32
33
34
35
36
37
38
39
40
41
42
43
44
45
46
47
48
49
50
51
52
53
54
55
56
57
58
59
60

Fig. 2. HiRISE orbital overview of the NASA Mars Science Laboratory Curiosity rover's traverse from Bradbury Landing up to sol 2359. Select locations are annotated as well as sol 1809 when Curiosity ascended on to Vera Rubin ridge (VRR), and sol 2302 when Curiosity traversed off VRR and into the Clay Bearing Unit. Adapted image from NASA-JPL/Fraeman.

190x275mm (300 x 300 DPI)

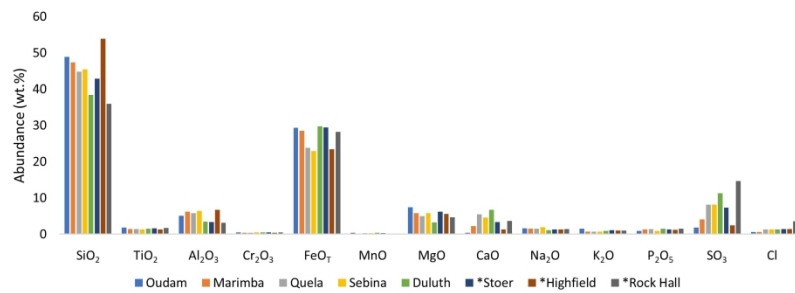


Fig. 3. Main-phase alteration assemblage compositions for Oudam, Marimba, Quela, Sebina, Duluth, Stoer, Highfield and Rock Hall. Calculated using APXS and CheMin results (Achilles et al., 2020; Rampe et al., 2020b), as explained in hypothesis and model set-up section "Host Rock Composition". Samples Oudam, Marimba, Quela, Sebina, and Duluth are from pre-VRR Murray formation localities. Stoer, Highfield and Rock Hall represent VRR Murray. *indicates drill samples acquired from VRR.

190x275mm (300 x 300 DPI)

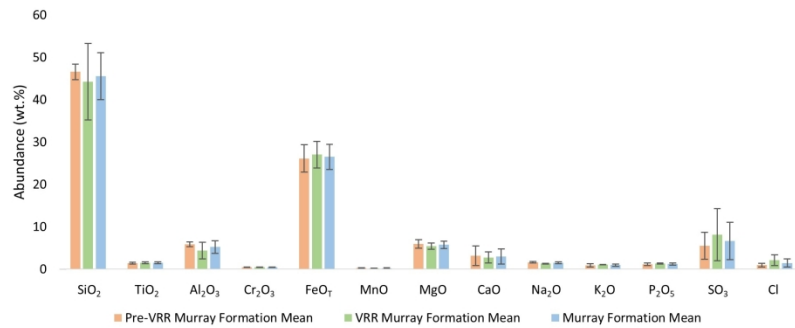


Fig. 4. Mean alteration compositions for the Pre-VRR Murray formation (Oudam, Marimba, Quela, Sebina), VRR Murray Formation (Stoer, Highfield and Rock Hall), the overall Murray Formation. Calculated using APXS and CheMin results. Error bars show standard deviation for each calculated mean, illustrating the statistical similarity between the calculated alteration compositions.

190x275mm (300 x 300 DPI)

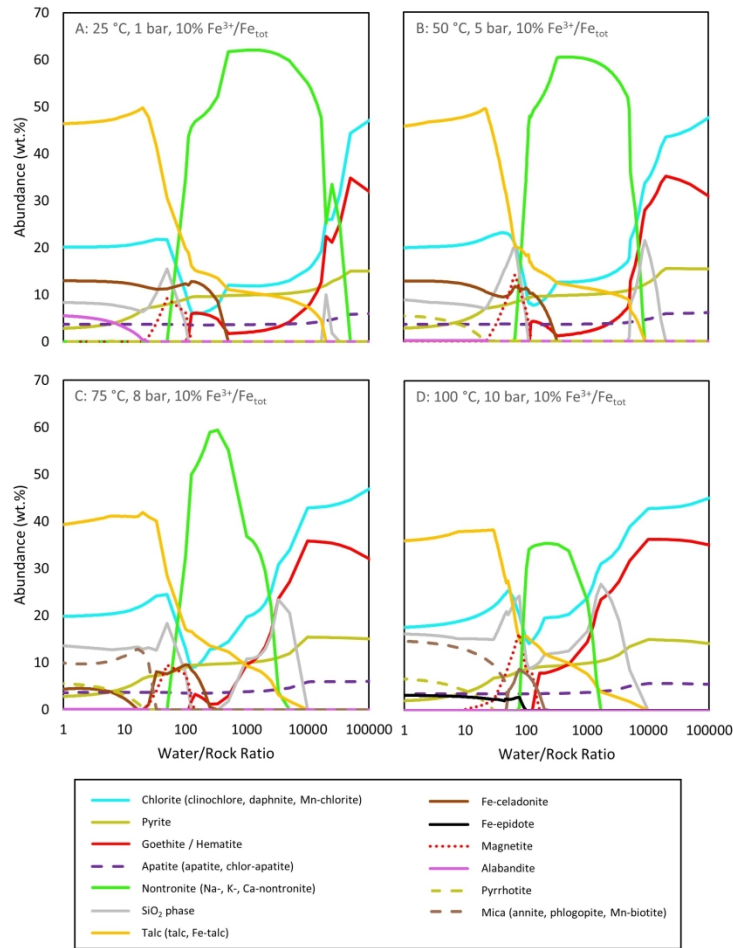


Fig. 5. CHIM-XPT results for the calculated VRR alteration composition (Table S4) reacted with GPW (Bridges et al., 2015b). Reactions at 25, 50, 75 and 100 °C, and 10% of the FeOT is Fe³⁺, as indicated. Goethite only precipitated at 25 °C (A), and hematite did not precipitate at that temperature. K-nontronite precipitated at 25 °C (A), whereas Na-nontronite did not precipitate at 100 °C (D) and Ca-nontronite precipitated at all temperatures. Chlor-apatite formed at 25 °C (A), 50 °C (B) and 75 °C (C), whereas apatite formed at 75 °C (C) and 100 °C (D). Trace abundances of calcite, spurrite and merwinite are not included on the plots.

190x275mm (300 x 300 DPI)

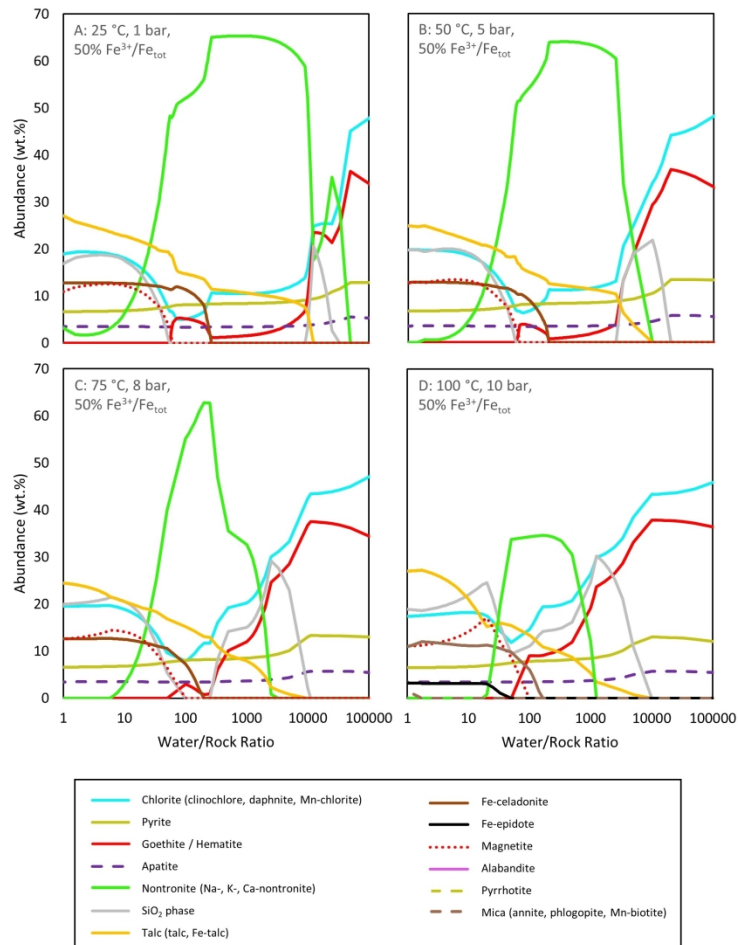


Fig. 6. CHIM-XPT results for the calculated VRR alteration composition (Table S4) reacted with GPW (Bridges et al., 2015b). Reactions at 25, 50, 75 and 100 °C, and 50% of the FeOT is Fe³⁺, as indicated. Goethite only precipitated at 25 °C (A), and hematite did not precipitate at that temperature. K-nontronite precipitated at 25 °C (A) and 50°C (B), whereas Na-nontronite did not precipitate at 100 °C (D) and Ca-nontronite precipitated at all temperatures. Rhodochrosite precipitated at 25 °C (A) and 50 °C (B), and trace wt.% of calcite precipitated at all temperatures for 50% Fe³⁺/Fe_{tot} (A,B,C,D). Trace abundances of calcite, rhodochrosite, spurrite and merwinite are not included on the plots.

190x275mm (300 x 300 DPI)

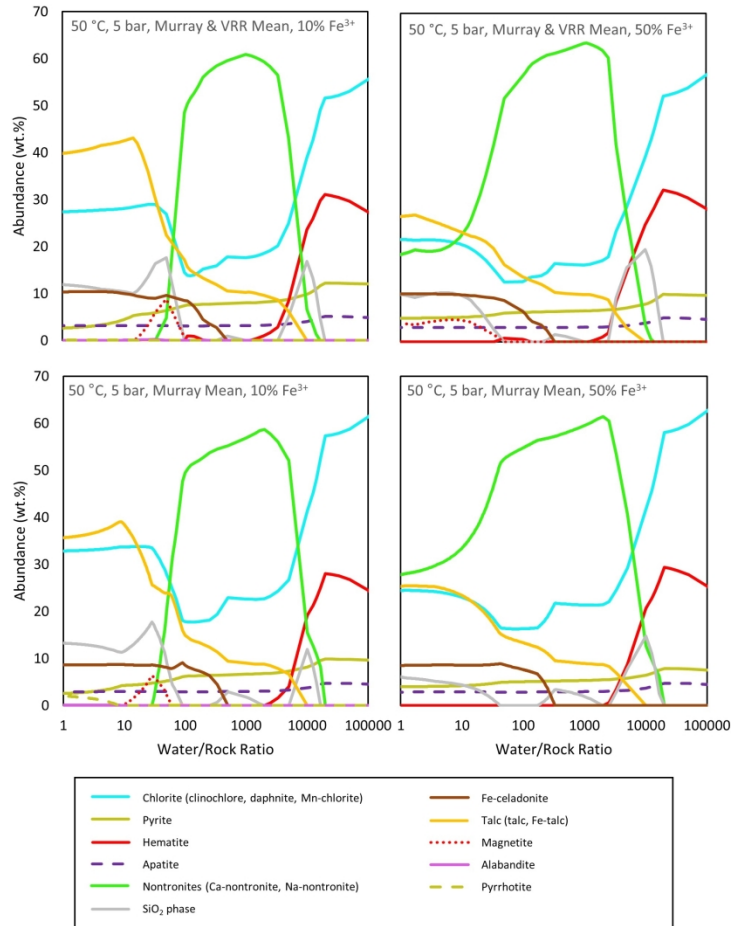


Fig. 7. CHIM-XPT results for the calculated alteration composition for the Murray formation and the Murray and VRR (overall) (Table S4) reacted with GPW (Bridges et al., 2015b). Reactions are at 50 °C and the Fe³⁺ content of FeOT is at 10% and 50%, as indicated. Trace abundances of rhodochrosite, calcite, spurrite and merwinite are not included on the plot.

190x275mm (300 x 300 DPI)

1
2
3
4
5
6
7
8
9
10
11
12
13
14
15
16
17
18
19
20
21
22
23
24
25
26
27
28
29
30
31
32
33
34
35
36
37
38
39
40
41
42
43
44
45
46
47
48
49
50
51
52
53
54
55
56
57
58
59
60

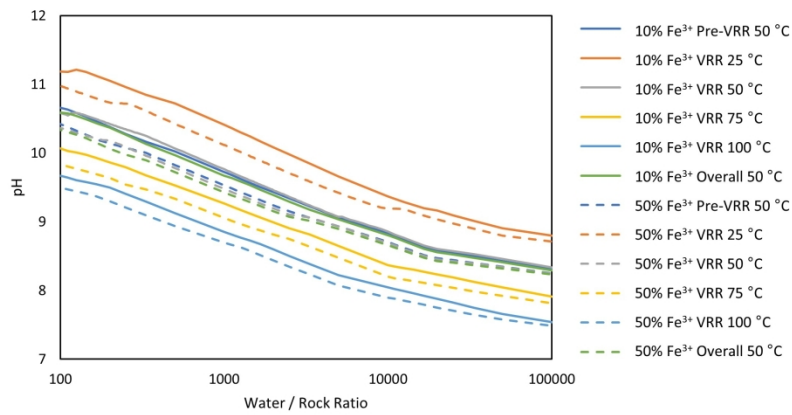


Fig. 8. Plot showing pH variation with W/R for the CHIM-XPT models shown in Fig. 5 – 7. Starting compositions for Pre-VRR Murray, VRR Murray and Overall Murray used in the modeling are shown in Table S4.

190x275mm (300 x 300 DPI)

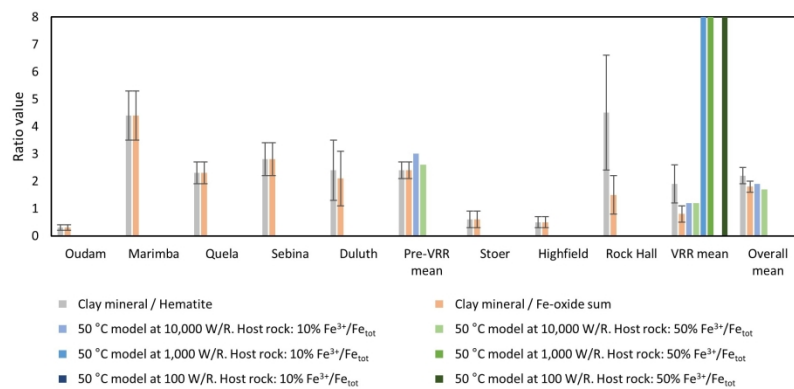


Fig. 9. Plot comparing calculated clay mineral / hematite and clay mineral / Fe-oxide sum for drill samples in the pre-VRR Murray formation and VRR, determined using CheMin wt.% mineral abundances (Achilles et al., 2020; Rampe et al., 2020b). Means are included for pre-VRR and VRR samples, as well as an overall mean. Errors shown are propagated errors calculated from errors in mineral abundances. Values for models run at 50 °C at 10,000 W/R, 1,000 W/R and 100 W/R from Tables 2 and 3 are included for comparison.

190x275mm (300 x 300 DPI)

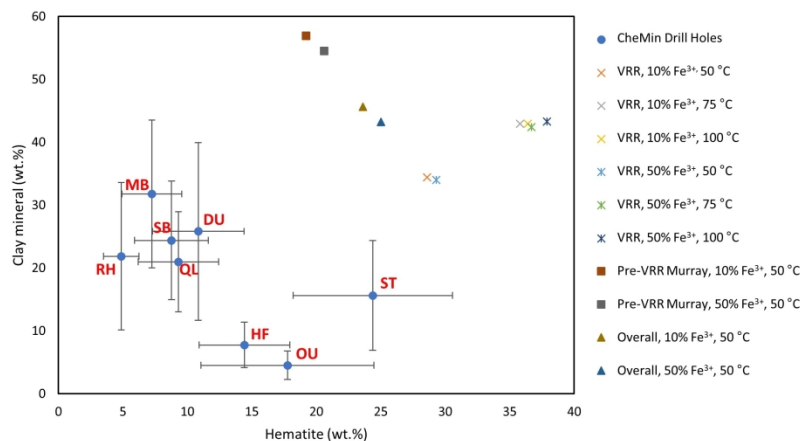


Fig. 10. Clay mineral abundance vs hematite abundance from CheMin (Achilles et al., 2020; Rampe et al., 2020b) normalized to the alteration component (including amorphous phase) compared to CHIM-XPT results in this study (Fig. 5 – 7; Tables S5 and S8) at high (10,000) W/R. Drill holes Oudam, Marimba, Quela, Sebina, Duluth, Stoer, Highfield and Rock Hall are annotated with OU, MB, QL, SB, DU, ST, HF and RH, respectively. Linear regression carried out on thermochemical models at 50 °C in the Fig. revealed the trend $y = (-2.35 \pm 0.09)x + (102.15 \pm 2.16)$ with an R^2 value of 0.99. Comparative linear regression carried out on CheMin drill samples Oudam, Marimba, Sebina, Quela, Duluth, Highfield and Rock Hall in the Fig. gave a trend of $y = (-1.88 \pm 0.56)x + (39.23 \pm 6.24)$ with an R^2 value of 0.70. This trend changed to $y = (-2.56 \pm 0.45)x + (48.38 \pm 5.33)$ with an R^2 value of 0.89 with Rock Hall removed from the analysis.

190x275mm (300 x 300 DPI)

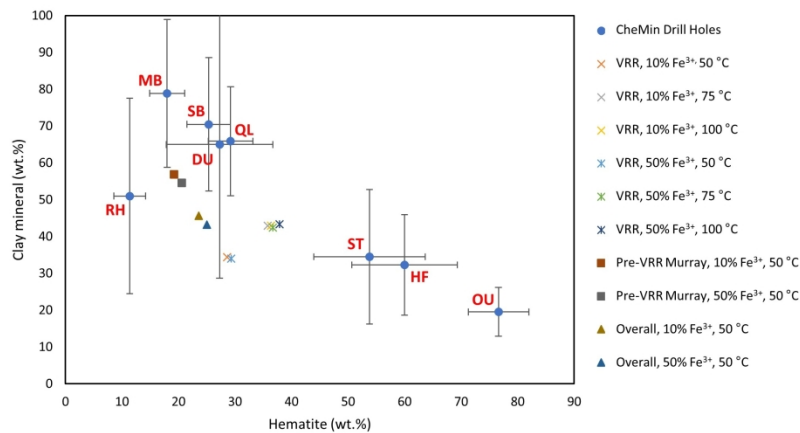


Fig. 11. Clay mineral abundance vs hematite abundance from CheMin (Achilles et al., 2020; Rampe et al., 2020b) normalized to the alteration component (excluding the amorphous component) compared to CHIM-XPT results in this study (Fig. 5 – 7; Tables S5 and S8) at high (10,000) W/R. The comparable negative correlations of different gradients for the CheMin drill holes and the thermochemical models and the trend with temperature shown in Fig. 10 indicates that only a part of the derived alteration composition is reactive. Drill hole names and abbreviations detailed in Fig. 10 caption.

190x275mm (300 x 300 DPI)

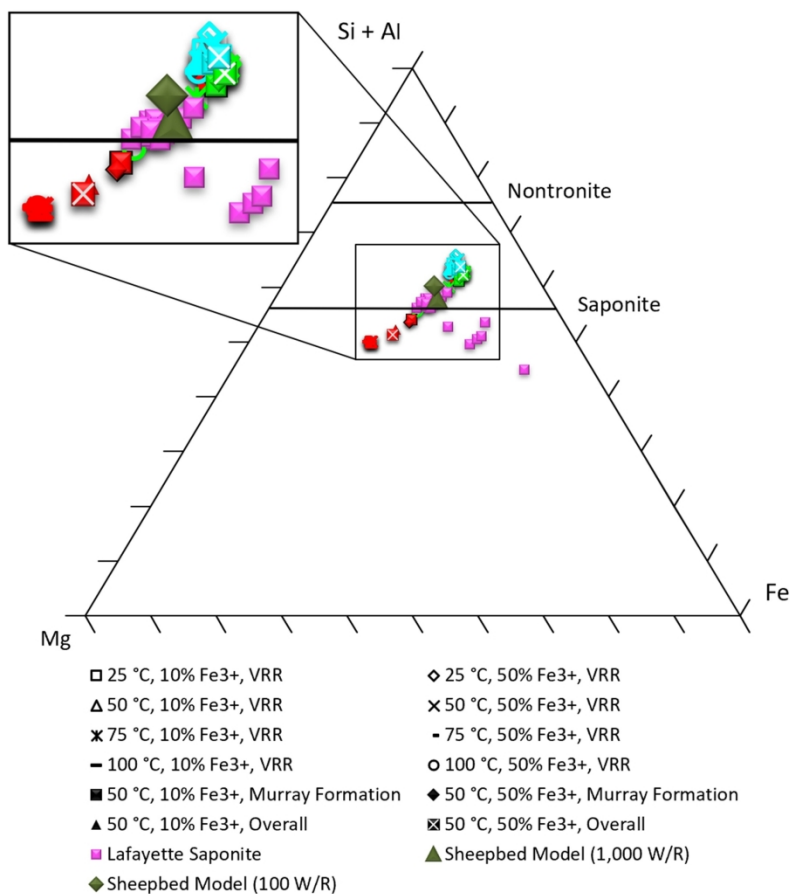


Fig. 12. Mg-Si+Al-Fe tot at. ternary plot. Results at 10,000 (red), 1,000 (green) and 100 (blue) W/R from the thermochemical models in this paper are plotted with some additional data from other sources for comparison. Lafayette saponite data taken from Hicks et al. (2014). CHIM-XPT results for the Sheepbed unit from Bridges et al. (2015b) at 100 W/R are shown for comparison.

190x275mm (300 x 300 DPI)